Bulletin of the Seismological Society of America, Vol. 108, No. 3B, pp. 1596–1622, July 2018, doi: 10.1785/0120170336

Ⓔ

Coseismic Rupture and Preliminary Slip Estimates for the Papatea Fault and Its Role in the 2016 M_w 7.8 Kaikōura, New Zealand, Earthquake

by Robert M. Langridge, Julie Rowland, Pilar Villamor, Joshu Mountjoy, Dougal B. Townsend, Edwin Nissen, Christopher Madugo, William F. Ries, Caleb Gasston, Albane Canva, Alexandra E. Hatem, and Ian Hamling

Abstract Coseismic rupture of the 19-km-long north-striking and west-dipping sinistral reverse Papatea fault and nearby structures and uplift/translation of the Papatea block are two of the exceptional components of the 14 November 2016 M_w 7.8 Kaikōura earthquake. The dual-stranded Papatea fault, comprising main (sinistral reverse) and western (dip-slip) strands, ruptured onshore and offshore from south of Waipapa Bay to George Stream in the north, bounding the eastern side of the Papatea block. Fault rupture mapping was aided by the acquisition of multibeam bathymetry, light detection and ranging (lidar) topography and other imagery, as well as differential lidar (D-lidar) from along the coast and Clarence River valley. On land, vertical throw and sinistral offset on the Papatea fault was assessed across an aperture of ±100 m using uncorrected D-lidar and field data to develop preliminary slip distributions. The maximum up-to-the-west throw on the main strand is ~9.5 ± 0.5 m, and the mean throw across the Papatea fault is ~4.5 ± 0.3 m. The maximum sinistral offset, measured near the coast on the main strand, is ~6.1 ± 0.5 m. From these data, and considering fault dip, we calculate a maximum net slip of 11.5 ± 2 m and an average net slip of 6.4 ± 0.2 m for the Papatea fault surface rupture in 2016. Large sinistral reverse displacement on the Papatea fault is consistent with uplift and southward escape of the Papatea block as observed from Interferometric Synthetic Aperture Radar (InSAR) and optical image correlation datasets. The throw and net slip are exceedingly high for the length of the Papatea fault; such large movements likely only occur during multifault Kaikōura-type earthquakes that conceivably have recurrence times of ≥ 5000–12,000 yrs. The role of the Papatea fault in the Kaikōura earthquake has significant implications for characterizing complex fault sources in seismic hazard models.

Electronic Supplement: Rupture descriptions for minor faults, figures of detailed bathymetry and vertical throw, far-field profiles of deformation, and surface rupture photographs, and table of site localities with fault and slip information.

Introduction

Based on the global record of historical earthquakes, multimeter coseismic displacements on crustal faults are associated with large ($M_w > 7$) to great ($M_w > 8$) earthquakes that typically occur on long faults or ruptures (e.g., Lin *et al.*, 2001; Barka *et al.*, 2002; Haeussler *et al.*, 2004; Rodgers and Little, 2006; Xu *et al.*, 2009; Yu *et al.*, 2010; Vallage *et al.*, 2015). These data are used to develop global scaling-relation parameters for seismic hazard, some of which are based on the coseismic slip values (e.g., Wells and Coppersmith, 1994). Paleoseismic studies that interrogate the slip from prehistoric earthquakes are used in conjunction with the scaling relationships to infer earthquake magnitudes from past large earthquakes. In this regard, the 14 November M_w 7.8 Kaikōura earthquake, with an along-strike length of 165 km of ground and seafloor surface rupture (Litchfield *et al.*, 2018), fits the expectation of large displacement on long, smooth, and straight high-slip-rate faults with short recurrence intervals, such as was observed on the Jordan and Kekerengu faults (Fig. 1; Kearse *et al.*, 2018; Little *et al.*, 2018). However, the Kaikōura earthquake was a complex event, reflected by

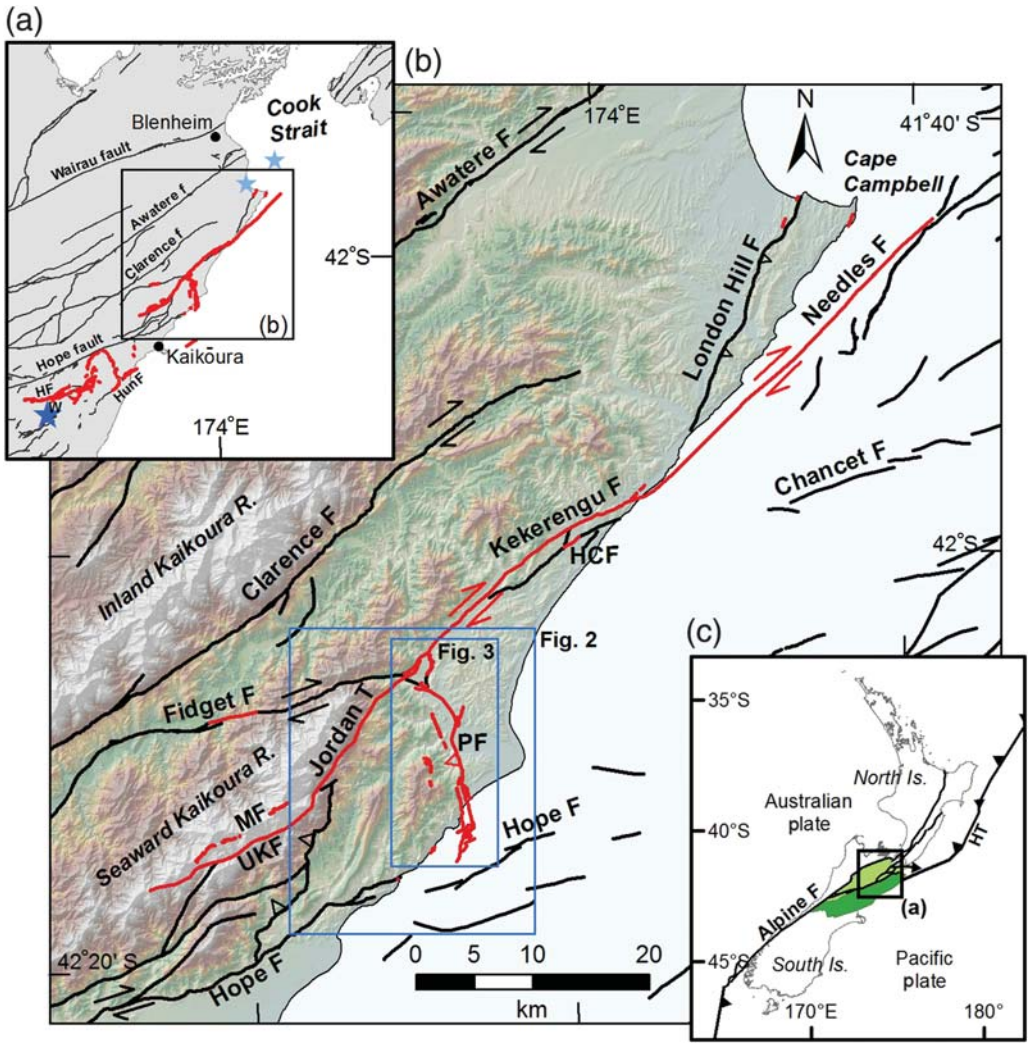

Figure 1. (a) Summary map of the 2016 M_w 7.8 Kaikōura earthquake ruptures (red), northeastern South Island. Other active faults that did not rupture in the 2016 earthquake are colored black. The earthquake epicenter (dark blue star) is near Waiau (W) in the southwest. The epicenters of the 2013 M_w 6.6 Cook Strait earthquakes are shown as light blue stars. HF, Humps fault; HunF, Hundalee fault. (b) Summary map of the Marlborough Fault System (MFS) fault ruptures and other active faults (after Langridge *et al.*, 2016, and Litchfield *et al.*, 2018). The area of Figures 2 and 3 are shown by blue boxes. HCF, Heavers Creek fault, MF, Manakau fault; PF, Papatea fault; UKF, Upper Kowhai fault; T, thrust. (c) Simplified plate tectonic map of New Zealand including the Alpine fault, MFS (light green), North Canterbury Domain (dark green), and Hikurangi subduction margin, represented by the Hikurangi trough (HT).

the surface rupture of a large number of faults with differing styles (including strike-slip and oblique-slip faults with both dextral- and sinistral-slip senses), fault lengths, and slip magnitudes (Litchfield *et al.*, 2018). These faults are distributed across two distinct seismotectonic provinces, the North Canterbury Domain (NCD) and the Marlborough Fault System (MFS), both of which are characterized by different strain rates occurring across a largely homogeneous Mesozoic basement sequence draped by Tertiary rocks and cut by Mesozoic to Tertiary structure (Rattenbury *et al.*, 2006; Litchfield *et al.*, 2014). One of the outstanding aspects of Kaikōura earthquake deformation that highlights its complexity was the exceedingly large uplift and south-directed transport of the Papatea block that occurred in association with coseismic rupture of a short and previously unknown active oblique-slip fault, the Papatea fault (Fig. 2; Clark *et al.*, 2017; Hamling *et al.*, 2017).

The purposes of this article are to: (1) introduce and document the 19-km-long Papatea fault surface rupture and other nearby related fault ruptures, (2) present preliminary coseismic slip distributions, (3) relate Papatea fault slip to seismic hazard considerations, and (4) reconcile fault motions with the large uplift and motion associated with the Papatea block. Rupture of the oblique-slip Papatea fault is associated with onshore and offshore faulting, coastal and block uplift, subsidiary fault ruptures, very large landslides, and avulsion of the Clarence River. The Papatea fault is associated with some of the largest coseismic displacements and deformation in the Kaikōura earthquake, equivalent to

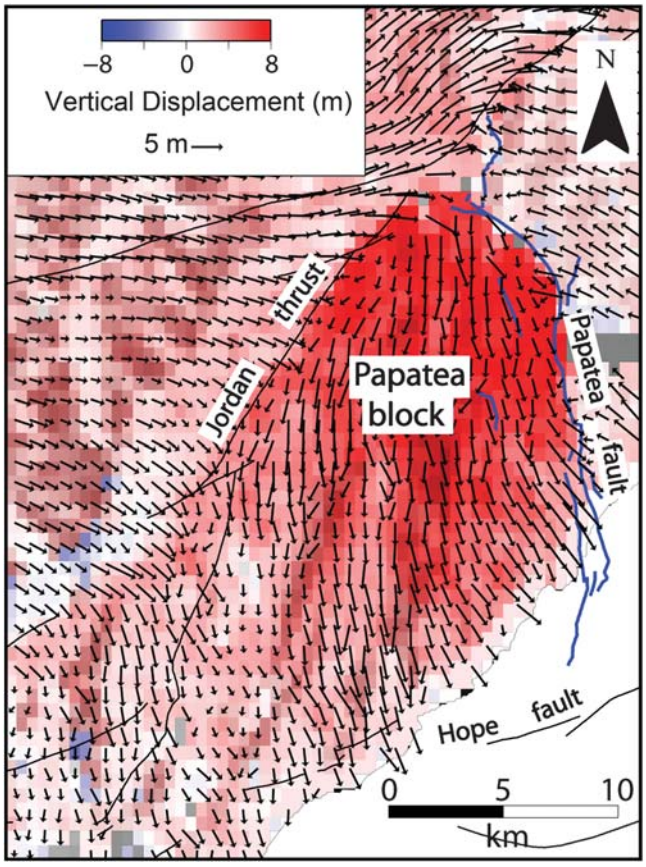

Figure 2. The 3D displacement field over the Papatea block in the 2016 Kaikōura earthquake derived from radar amplitude offsets (modified from Hamling *et al.*, 2017). Blue lines represent fault ruptures described in this article, including the Papatea fault. Arrows represent the horizontal vectors and displacement, and the background shows the vertical displacements.

those observed on the Kekerengu fault, which had a maximum surface displacement of ~12 m (Kearse *et al.*, 2018; Litchfield *et al.*, 2018). The multimeter scale of vertical and lateral displacement on the Papatea fault motivates the comparison of fault length versus displacement with respect to other historical earthquake examples (e.g., Lin *et al.*, 2001; Rodgers and Little, 2006; Yu *et al.*, 2010; Vallage *et al.*, 2015). In this study, we have been able to map surface ruptures of the Papatea and nearby faults precisely both on land to the coast and offshore, using multiple cutting-edge high-precision techniques, making this one of the best mapped offshore-to-onshore fault ruptures globally (see also Kearse *et al.*, 2018). This article documents fault ruptures from post-earthquake field-based mapping and digital survey-derived datasets, including multibeam and green-band offshore and differential light detection and ranging (D-lidar) onshore, to produce preliminary slip distributions for the Papatea fault. Understanding the Papatea fault and associated block motions provides important insights into complex fault ruptures and their characterization for seismic hazard purposes.

Overview of the Kaikōura Earthquake

The 14 November 2016 M_w 7.8 Kaikōura earthquake, in the northern part of the South Island of New Zealand, was one of the largest and most complex on-land earthquakes observed historically (Hamling *et al.*, 2017; Litchfield *et al.*, 2018). The earthquake initiated at 00:02 local time at a depth of 15 km with an oblique-thrust mechanism and an epicenter ~30 km inland from the coast (Fig. 1a; Kaiser *et al.*, 2017). The Kaikōura earthquake comprised several subevents involving crustal faults (Duputel and Rivera, 2017; Holden *et al.*, 2017) and possibly a deeper low-angle fault or subduction interface source, as inferred from seismologic and tsunami modeling (Bai *et al.*, 2017; Cesca *et al.*, 2017; Furlong and Herman, 2017; Wang *et al.*, 2018). The earthquake rupture generally propagated from the epicenter near Waiau northeastward to beyond Cape Campbell over a strike length of ~165 km. It included rupture of on-land and submarine faults, extensive coseismic uplift across 110 km of the coastline, and generation of tsunami (Clark *et al.*, 2017; Power *et al.*, 2017; Stirling *et al.*, 2017).

The Kaikōura earthquake involved motion on an unprecedented number of crustal faults. Surface rupture of ≥ 1.5 m occurred on 13 faults, and localized minor displacement (≤ 1.5 m) occurred on at least another 11 faults (Litchfield *et al.*, 2018). The faults that ruptured in the Kaikōura earthquake span the transition between oblique subduction of the Pacific plate along the Hikurangi subduction margin (HSM) to the northeast, and continental collision along the transpressional Alpine fault to the southwest (Fig. 1c; Wallace *et al.*, 2007, 2012). This transition zone can be divided into several tectonic domains, based on their differing fault kinematics and slip rates (Stirling *et al.*, 2012; Litchfield *et al.*, 2014). The rupture zone extended from the relatively low-strain rate, predominantly contractional NCD domain, rupturing the Humps, Leader, Hundalee, and other faults (Pettinga *et al.*, 2001; Barrell and Townsend, 2012; Nicol *et al.*, 2018; Williams *et al.*, 2018) northeastward into the higher-strain-rate dextral strike-slip MFS domain (Fig. 1b), rupturing the Jordan thrust, Upper Kowhai, Kekerengu, Needles, and other faults (Van Dissen and Yeats, 1991; Kearse *et al.*, 2018). Several of the faults that ruptured in 2016, including the Papatea fault, were not previously recognized as active faults in the New Zealand Active Faults Database (NZAFD; Langridge *et al.*, 2016).

Geology and Definition of the Papatea Fault

The sinuous but overall north-striking sinistral reverse (i.e., sinistral < reverse) Papatea fault takes its name from the stream that emerges on the coast northeast of Waipapa Bay (Fig. 3). The west-dipping Papatea fault extends from offshore of Waipapa Bay in the south to George Stream in the north, where it projects toward the Jordan thrust (Van Dissen and Yeats, 1991; Kearse *et al.*, 2018). The Papatea fault defines the eastern margin of an unnamed range

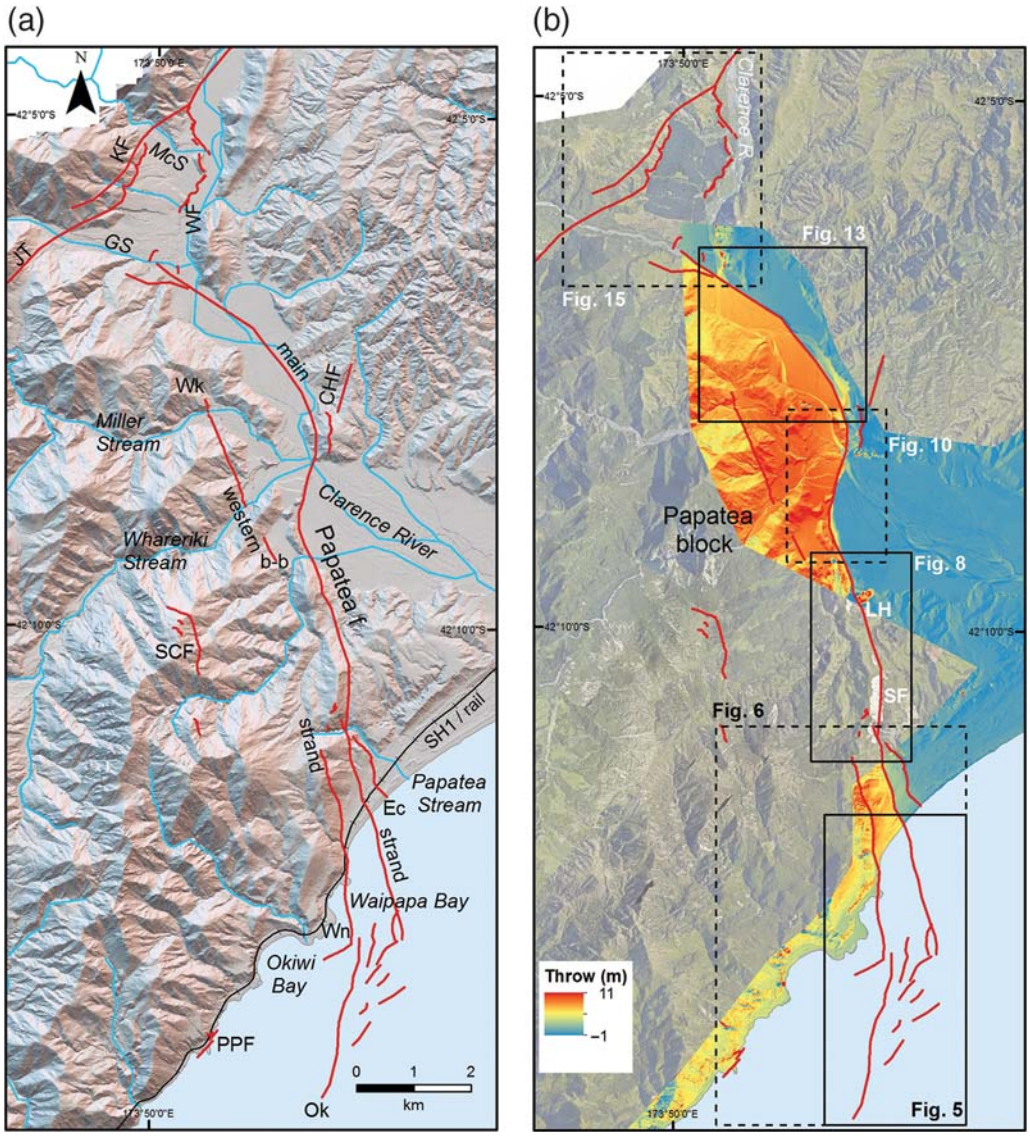

Figure 3. Location maps and summary of remote sensing data sources used to map the Papatea and other faults and to determine fault offsets. Fault mapping shown at a scale of 1:250,000. (a) Postearthquake light detection and ranging (lidar) hillshade model indicating the major geographic features and rupture strands. Ok, Okiwi; Wn, Wainui; b-b, back-basin; Wk, Wharekiri; Ec, Edgecombe traces of the Papatea fault; PPF, Paparoa Point fault; SCF, Stewart Creek fault; KF, Kekerengu fault; WF, Waiautoa fault; JT, Jordan thrust; GS, George; and McS, McLean streams. (b) Postearthquake color orthophoto mosaic overlain by the area of differential lidar (D-lidar) coverage along the coast and in the lower Clarence Valley. Scale shows the magnitude of vertical throw from D-lidar across the Papatea fault, shown in meters above pre-earthquake lidar dataset. Color orthophoto highlights the Seafront (SF) and Limestone Hills (LH) landslide scars (white areas). Boxes indicate the areas of detailed fault maps.

in the hanging wall of the fault, termed the Papatea block after Hamling *et al.* (2017). In this article, we define the Papatea fault, from its surface rupture pattern in 2016, as comprising a dual-stranded fault with a main (eastern) strand and a western strand. A third minor (Edgecombe) trace occurs at the coast (Fig. 3a). This article also documents two other faults occurring in the footwall of the Papatea fault (Waiautoa and Corner Hill faults), and the Stewart Creek (SCF) fault, a short fault within the hanging-wall block, because these faults are related to the wider deformation associated with the Papatea fault and block (see Ⓔ the electronic supplement to this article).

The geology of the hanging-wall block of the Papatea fault is characterized by a tightly folded sequence of Early Cretaceous Pahau terrane metasedimentary basement rocks, dominated by graywacke, overlain by a cover rock sequence that includes Mid-to-Late Cretaceous sandstones and Paleocene to Oligocene limestones (Fig. 4; Rattenbury *et al.*, 2006). The hanging-wall Papatea block includes rugged hill-country formed in the Pahau basement and a relatively lower

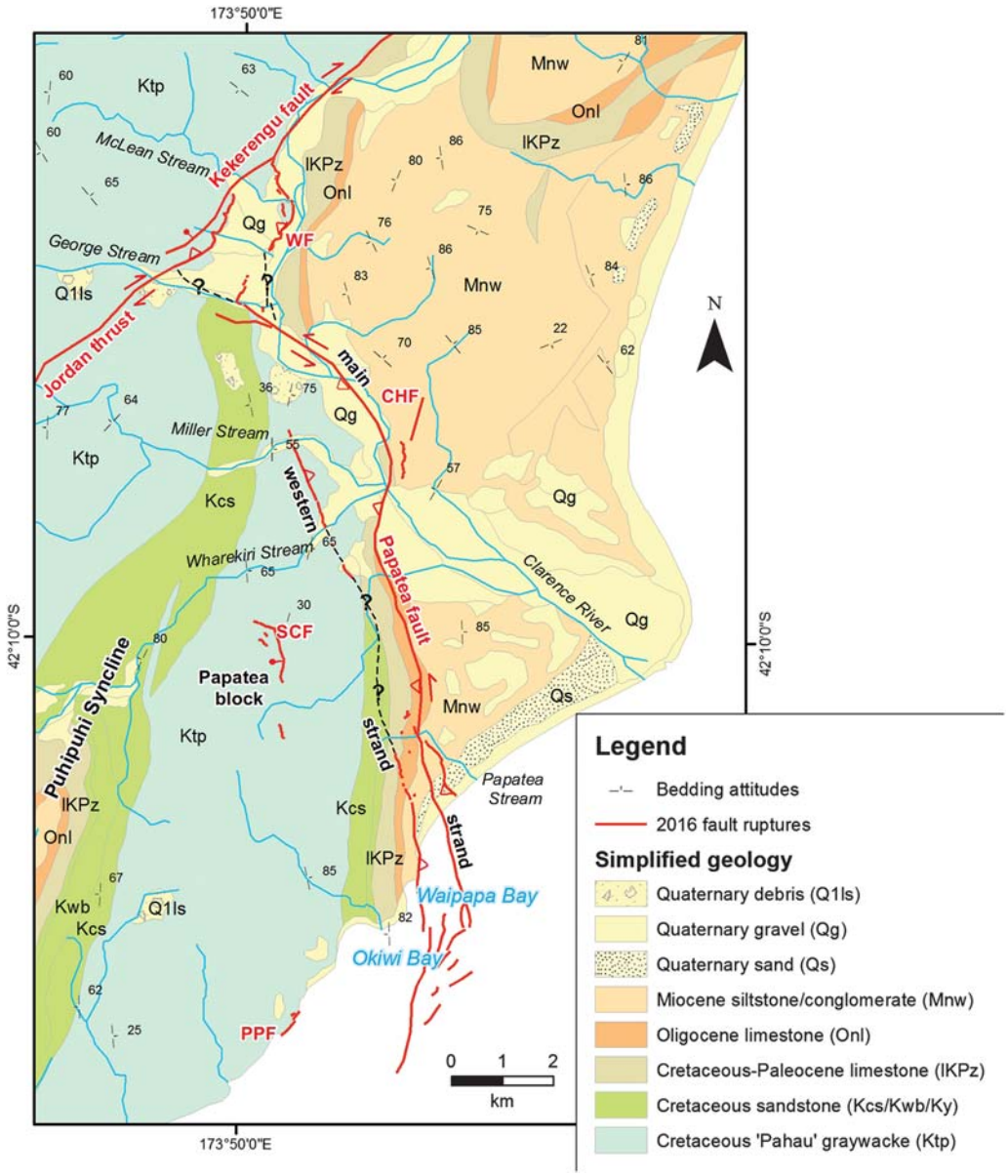

Figure 4. Simplified geological map of the lower Clarence Valley area including representative bedding attitudes (after Rattenbury *et al.*, 2006). The 2016 Kaikōura earthquake fault ruptures are shown in red, highlighting the Papatea and other faults, including the Corner Hill fault (CHF), PPF, SCF, and WF. Interpreted geologic extensions of the main and western strands of the Papatea fault and WF that did not show ground surface rupture in 2016 are shown by black dashed lines.

valley underlain by tightly folded sedimentary cover rocks preserved in the Puhipuhi Syncline (Van Dissen and Yeats, 1991). Limestones within the cover rock sequence are relatively erosion resistant and form prominent strike ridges in the landscape. This suite of cover rocks is exposed with subvertical dips on the eastern edge of the Papatea block. Three lithologies, the Muzzle Group limestones (Cretaceous–Paleocene; lKPz), Motunau Group limestones (Oligocene; Onl), and Waima Formation (Early Miocene; Mnw), have been identified in fault and landslide exposures and appear to be the most useful rocks to track the structure of the Papatea fault (Fig. 4). A similar, though less deformed sequence of rocks draped by Pliocene and Quaternary deposits crop out to the east on the footwall side of the Papatea fault.

Structurally, the Papatea block can be thought of as a paired north-northeast-trending syncline–anticline structure bounded and truncated in the northwest by the northeast-striking Jordan thrust, the gently curving, north-striking Papatea fault in the east, and in the south by the east-northeast-striking Hope fault (Figs. 1b and 3). In the footwall block, the predominant bedrock unit at the surface is Early to Mid-Miocene Waima Formation, overlain by undifferentiated Pliocene rocks and late Quaternary alluvial and coastal deposits (marine oxygen isotope stages 1–7; Rattenbury

et al., 2006). The tectonic fabric (e.g., folds and strike ridges) described earlier is considered to be post-Waima (Middle Miocene) in age.

Prior to the Kaikōura earthquake, a pair of subparallel north-striking bedrock faults had been mapped parallel to bedding contacts along the eastern range front of the Papatea block (Rattenbury *et al.*, 2006). Barrell (2015) indicates these faults, naming them the Papatea faults, as possibly active faults in a local fault compilation. At that time, the Papatea faults were not included in the NZAFD (Langridge *et al.*, 2016), due to a lack of evidence of their activity. The 2016 coseismic ruptures on the main and western strands of the Papatea fault (as defined here) do not, however, correlate directly with the formerly defined structure and instead cut obliquely across the Tertiary bedrock structure. Earlier mapping by Lensen (1962) is more consistent with this structure. Lensen clearly shows the main strand crosscutting steeply dipping late Cretaceous to Tertiary structure (broadly in the location of the 2016 rupture) and additionally shows a fault at the location of the Wainui trace on the coastal platform. North of Corner Hill and its northern crossing of the Clarence River, the structure of the Papatea fault was not clear before the earthquake (Lensen, 1962; Rattenbury *et al.*, 2006). However, what is clear from those maps is that there is typically no Early Cretaceous Pahau terrane graywacke exposed to the north and east of the Papatea fault in the footwall block and that the belt of steeply dipping Mid-Cretaceous to Early Miocene rocks observed south of the Clarence River is repeated to the north of the Papatea fault (Fig. 4).

Thus, the sinistral reverse Papatea fault is defined here as (1) an important active bedrock structure with two major strands that ruptured in the 2016 Kaikōura earthquake; (2) a north-striking fault that obliquely crosscuts regional geology in the south and which swings to the northwest in the north, truncating major Tertiary structures, such as the Puhipuhi Syncline (Van Dissen and Yeats, 1991); (3) a fault with a long-term record of reverse motion as evidenced from uplift of the Pahau basement-cored hanging-wall Papatea block (with a corresponding lack of exposure of these rocks on its footwall); and (4) a fault with a significant record of apparent sinistral motion, as evidenced from the lateral separation of the steeply dipping cover rock sequence to the south and north of the Clarence River. The large-scale geomorphology of the oblique-slip Papatea fault has elements of both a reverse fault, because it has high topography that thrusts older rocks and hill country over younger rocks and lower landscapes, and a strike-slip fault, because it acts to produce a fault-parallel valley where bedrock is laterally offset (Fig. 4).

Methods

Following the Kaikōura earthquake, significant oblique-slip fault ruptures were recognized during helicopter reconnaissance near the Clarence coastline, due to the severing of the highway and rail links, and from uplift of the coast. Field teams established that the Papatea fault had ruptured both onshore and offshore with large vertical and lateral movements (Figs. 3b and 5; Clark *et al.*, 2017; Stirling *et al.*, 2017; Litchfield *et al.*, 2018). Figures 6–16 provide documentation of the Papatea and nearby fault ruptures through maps, photographs, and profiles of vertical throw, from which preliminary coseismic slip distributions for throw and sinistral motion have been developed (Fig. 17).

Fault Rupture Mapping

To map the offshore part of the fault, the RV Ikatere was deployed to survey as close to the shoreline as possible. The offshore survey utilized a Kongsberg EM2040 multibeam echosounder system, an Applanix POS/MV 320 motion sensor (> 20 m water depth), and a PS120 ToPAS parametric sub-bottom profiler. The multibeam data were processed in CARIS HIPS to a grid resolution of between 0.5 and 2 m, depending on water depth. Figure 5 presents an uninterpreted near-shore and submarine image, highlighting the sharp definition of bedrock platforms and recent fault rupture traces offshore. These data, along with the acquisition of green-band lidar in the inshore area along the coast (50 cm digital elevation model [DEM]), have allowed for the detailed mapping of fault ruptures and the measurement of vertical displacement offshore (Fig. 6). The primary traces of the fault on the seafloor can be confirmed as being coseismic (2016) ruptures because they correlate with fresh coastal scarps, and they are present as angular scarps in the shallow-water mobile-sediment zone where they would not be preserved as seafloor features for a long time period (see Ⓔ Fig. S1).

On land, initial data collection involved locating surface fault ruptures and surveying critical offsets that were subject to rapid repair (e.g., transport links and farm features) or erosion (e.g., beach berms and river scarps). Figure 3 shows key remote sensing datasets used to map ground surface ruptures: a 50-cm postearthquake airborne lidar hillshade model, a regional composite orthophotograph, and a 1-m D-lidar dataset. Traditional field techniques (e.g., tape, compass, and hand-held Global Positioning System [GPS]) were aided by Unmanned Aerial Vehicle (drone), total-station, and Real Time Kinematic (RTK)-GPS surveys of cultural features (e.g., fencelines and roads) to estimate horizontal offsets. Regional scale airborne lidar and orthophotograph imagery were used to verify and improve the locations of fault traces from a scale of 1:250,000 to 1:5000 and to assess other displaced features not visited in the field. The acquisition of pre-earthquake lidar in the Clarence Valley in 2012 meant that a significant proportion of the Papatea fault could be mapped using vertical D-lidar (Fig. 3b), that is, a D-lidar dataset that is not corrected for horizontal motions. Some fault ruptures, for example, the Wharekiri trace on the western strand, were only recognized once D-lidar became available months after the earthquake.

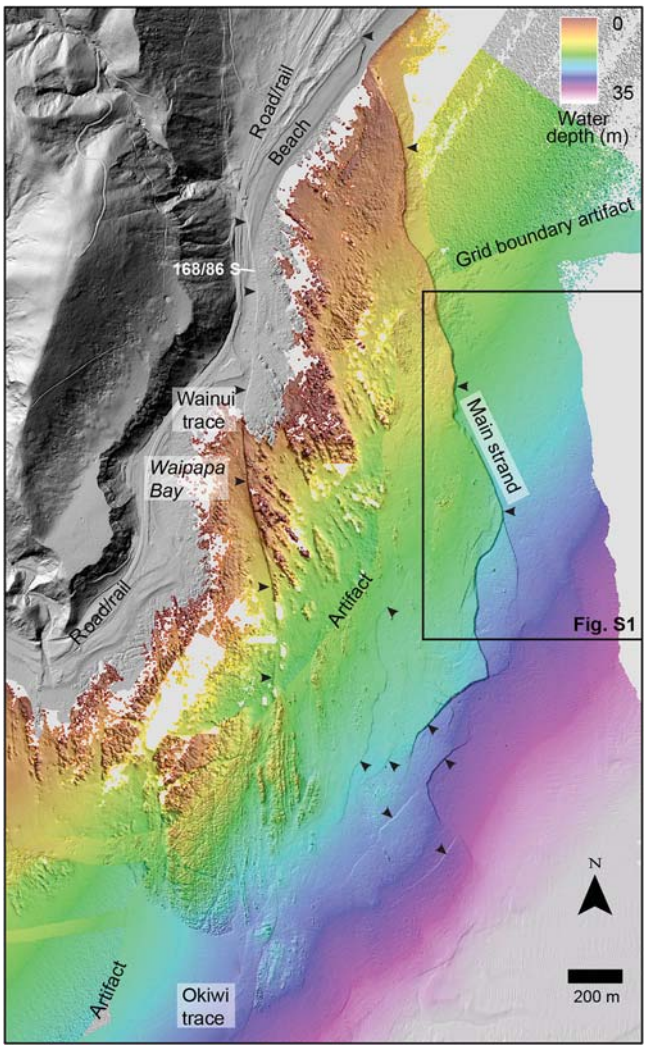

Figure 5. Uninterpreted postearthquake elevation (hillshade) and bathymetry (depth) model of the onshore-to-offshore transition of the Papatea fault (the location is shown in Fig. 3b). The main strand and important traces of the Papatea fault are indicated by black arrowheads. Offshore data sources are green-band lidar in the near-shore zone and multibeam echosounder data farther offshore. Box marks the area of Ⓔ Figure S1. See Figure 6 and Ⓔ Figure S1 (available in the electronic supplement) for interpretation and detail.

Collation of Coseismic Slip Data

A major objective of this article is to present preliminary coseismic slip distributions incorporating vertical throw and sinistral offset data (Fig. 17). The slip distribution for the Papatea fault comes from throw and sinistral offset data presented in Ⓔ Table S1. We assessed the net slip in one profile across the Papatea fault, derived from a combination of the throw, strike-slip offset, shortening, and dip angle for the main strand of the fault, minus the equivalent slip on the nearby western strand.

Vertical Throw

The scale of deformation across the oblique-slip Papatea fault provided some unique challenges in terms of assessing coseismic slip at the ground surface and seafloor. Coseismic vertical throws were some of the largest ever recorded on land, with a 5–6-km-long stretch of the main strand having ≥ 6 m up-to-the-west throw. Because of the rapid nature of the field reconnaissance, throw measurements were often estimated. However, because of the scale of single-event throw, these would typically underestimate throw due to compound (multiple) reverse scarps, or near to midfield warping of the ground surface. Because of this, our main method for assessing throw was to use D-lidar profiles of 200 m width across the fault zone, with field data as a comparative tool.

Following the reconnaissance field work, a 1-m resolution D-lidar dataset was developed and used for assessing the magnitude of vertical throw along the fault. To develop a slip distribution of throw, profiles perpendicular to the fault traces were made 100 m apart and checked using a semicontinuous point analysis in a Geographic Information System. We used a simple subtraction of the 2012 terrain from the 2016 terrain, that reveals vertical elevation changes at the raw resolution of the DEMs, as the primary basis for measuring vertical throw (Figs. 6 and 10). We acknowledge that this approach does not account for lateral motions that may produce apparent vertical throw where the slope of the land is significant, that is, the translation of topography will tend to produce apparent uplift or subsidence of features depending on their aspect and orientation relative to the displacement direction. Therefore, we also checked the vertical component of the 3D displacement field, generated using a windowed 3D registration of the pre- and postevent point clouds called an iterative closest point (ICP) analysis (Nissen *et al.*, 2012, 2017) that accounts for horizontal deformation but at the loss of spatial resolution. While we present here the uncorrected D-lidar results, the two approaches give results that are in close agreement, indicating that there is no systematic bias from lateral motions in the simple elevation change results. The ICP analysis highlights that, in most cases in which the topography is relatively flat (i.e., the coastal zone and throughout the Clarence Valley), the uncorrected D-lidar provides a suitable measure of throw. Details of the ICP analysis will be the subject of future research. Outside of areas that have D-lidar or offshore data coverage, for example, across the area of widespread landsliding, the throw is estimated from sparse postearthquake field observations. Because of the large and complex displacement pattern in such areas, we expect that these observations may underestimate the throw.

Sinistral Offsets

Sinistral offsets were assessed from field measurements using tape and compass, RTK-GPS surveys, and, in one case, a total-station survey. Additional measurements were developed from pre- and postearthquake imagery. The most common piercing lines were cultural features, especially fencelines. We also used roads, fruit tree lines, farm tracks, ditches, railway lines (e.g., Fig. 7c), and in some cases natural features (including dune and beach ridges, spurs, and

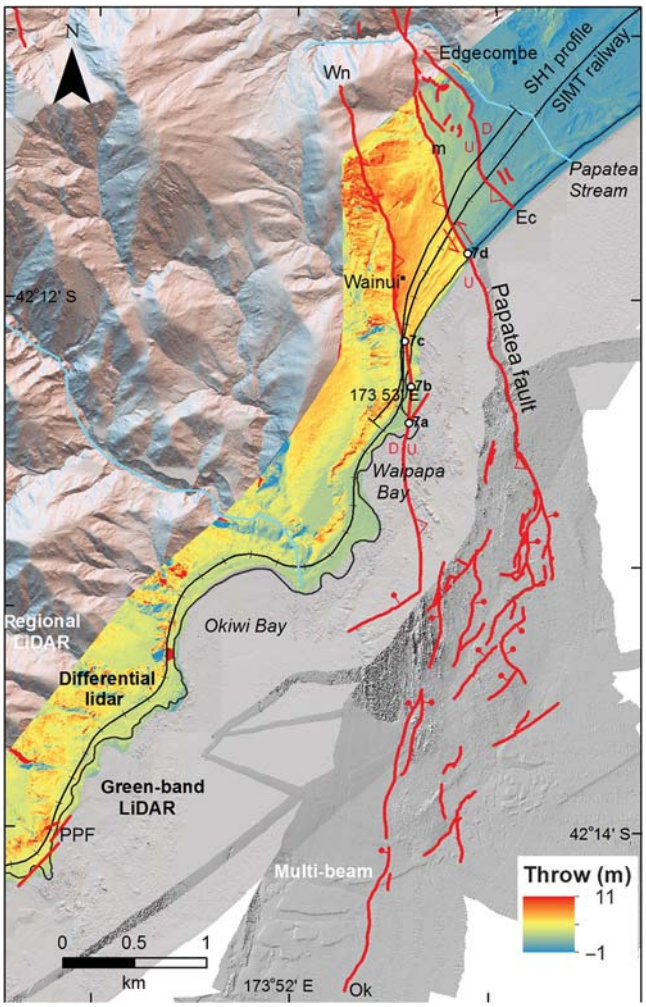

Figure 6. Detailed mapping at scale 1:5000 of the southern offshore and coastal part of the Papatea fault shown on digital shade models developed from postearthquake lidar, D-lidar, green-band lidar, and multibeam surveys (dark gray; the location is shown in Fig. 2b). m, main strand; Ok, Okiwi; Wn, Wainui; Ec, Edgecombe traces of the Papatea fault. Photo centers for Figure 7a–d are also shown. Fault sense shown by arrows, teeth, or bar and ball (for which sense is uncertain). State Highway 1 (SH1) profile is presented as Ⓔ Figure S2.

stream channels) to assess the horizontal offset. Where they cross the entire fault zone at a high angle, farm fencelines and the orchard lines were particularly good piercing lines with which to assess horizontal offsets. Our method for assessing the horizontal offset involved extrapolating the trend of a piercing line from some distance away into the fault zone (typically 100–200 m width as with throw) with the same trend used for the opposite side of the fault. This technique was performed in both directions and was effective for understanding the uncertainty of any measure where the piercing line was not, for example, originally straight (see Rockwell *et al.*, 2002; Little *et al.*, 2010; Kearse *et al.*, 2018). Because strike varies along the Papatea fault, offset was measured using the local strike within ∼100 m of the offset (Fig. 17; Ⓔ Table S1). Nonetheless, we accept that our analysis is limited to within ± ∼ 100 m of the fault (quasi-near-field) and may not reflect the total or distributed deformation across the wider fault damage zone (e.g., Vallage *et al.*, 2015). In some cases, we used pre-earthquake imagery in association with postearthquake lidar and imagery to estimate the scale of coseismic horizontal offset (e.g., on additional fencelines and a drain). In other cases, where piercing lines were absent (e.g., the stretch adjacent to Lake Murray) we created artificial pre- and postearthquake line markers from large reproducible features, for example, from the location of trees, bushes, and other farm features. These data were useful in supplementing the relatively sparse set of surveyed observations from field reconnaissance.

A significant uncertainty with measuring horizontal offsets from recent fault ruptures is the effect of apparent-versus-real offset (Kamb *et al.*, 1971; Mackenzie and Elliott, 2017). This uncertainty is especially relevant for oblique-slip faults that have a large component of throw or a shallow-to-intermediate fault dip. In addition, where a piercing line marker crosses the fault obliquely, it is likely that the true horizontal offset is diminished or enhanced, depending on its approach angle to the fault rupture. However, because of the scale of the offsets, this was deemed to be beyond the scope of this preliminary assessment of fault offset; therefore, we simply measured the sinistral offset measurements at face value; that is, we are only considering the measurement uncertainty.

Shortening

In addition to reverse and strike slip, the third component of motion in the fault slip vector comes from shortening, that is, the translation of the hanging-wall block across the fault. Shortening was recognized in the field by, for example, a freshly exposed thrust trace along the avulsed river course or more commonly by a slackened series of pickets in a fenceline. Mackenzie *et al.* (2017) indicate < 0.5 m of shortening in the field. For this preliminary assessment of offsets and fault slip, we have not directly assessed the shortening component along the length of the Papatea fault, due to the scale of deformation and difficulties in understanding the fault slip vector.

Fault Dip

Regional bedrock attitudes in the vicinity of the Papatea fault are typically too sparse near the fault traces and are likely to be the result of a complex deformational history dating from the Mesozoic to present (Fig. 4; Van Dissen and Yeats, 1991; Rattenbury *et al.*, 2006) to be of use in discerning the contemporary fault dip and kinematics of the Papatea fault.

The main rupture strand of the fault crops out in bedrock at the Clarence River below Corner Hill (attitude 009/51° W), where Paleocene Amuri limestone overthrusts Miocene Waima Formation across an ∼1-m-wide gouge zone

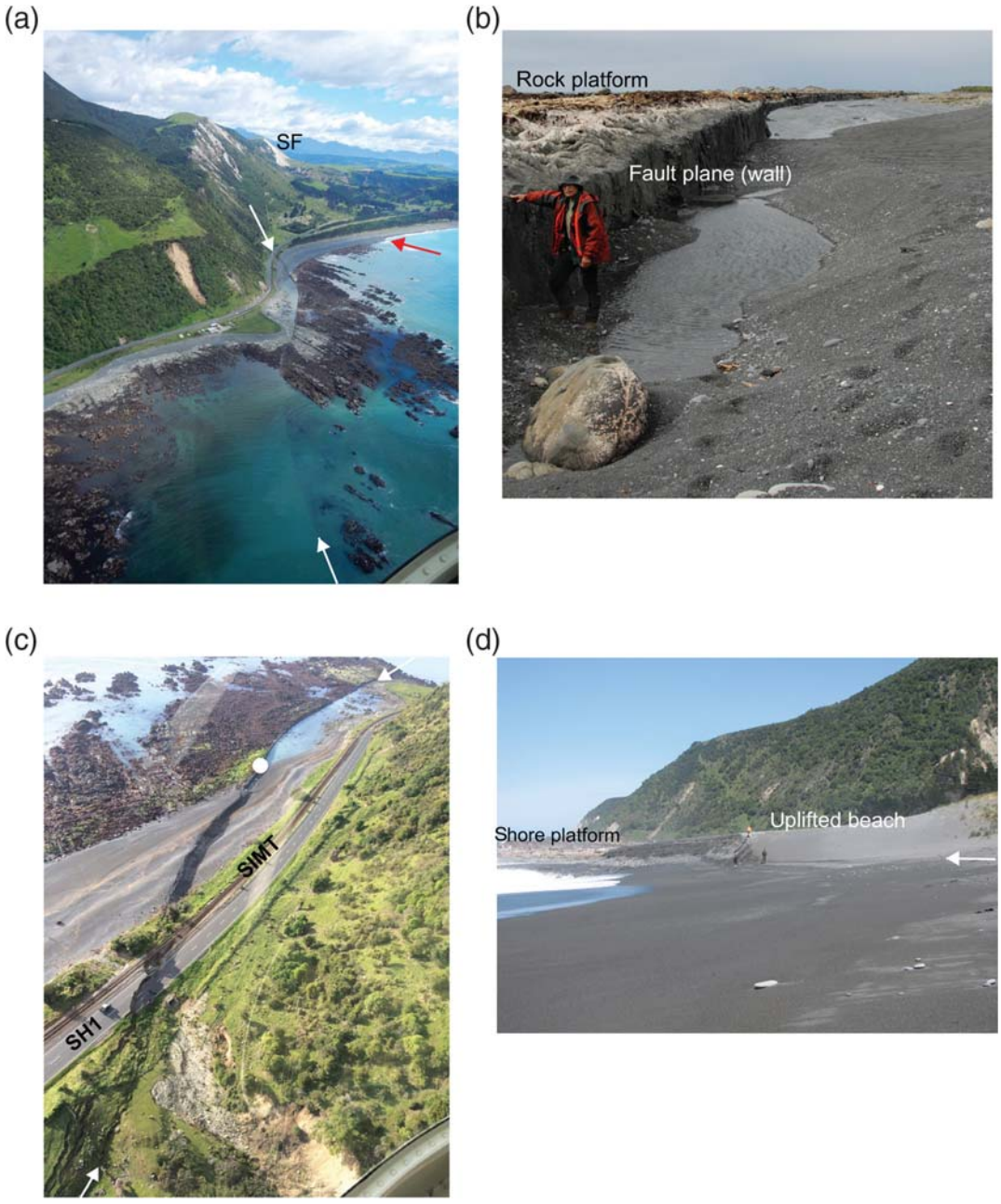

Figure 7. Photographs from the coastal portion of the Papatea fault (locations are shown in Fig. 6). (a) Aerial view along the western strand (Wainui trace; marked by white arrows). Red arrow points to (d) where the main strand of the fault intercepts the coastline. Seafront landslide (SF) scar in distance. (b) Exposed wall of fault gouge and uplifted shore platform (at top) along the Wainui trace. (c) The Wainui trace of the fault indicated by white arrows onshore crossing the shore platform, beach deposits, the railway (South Island Main Trunk [SIMT]) and highway (SH1). Location of photo in (b) is shown by white dot. (d) Five-meter high northeast-facing scarp of the main strand at the coast (marked by arrow), offsetting beach deposits and uplifting the shore platform, with people for scale.

(Fig. 11d). This dip value was confirmed using the geomorphic trace of the two mapped fault traces at Corner Hill to define the fault dip on either side of the wider fault zone from structure contours (Fig. 10).

While there are limited opportunities to assess the dip along the rupture zone, we recognize that the Papatea fault has a highly variable strike along its length, with significant strike changes occurring across relatively flat topography (Fig. 13). Therefore, we expect that the fault is also likely to have a variable dip, with steeper dips possible in areas where the strike is to the north or northwest. In other words, the fault exposures at Corner Hill where the strike is east of north may not be representative of the fault dip along strike. The fault plane may also have a variable dip with depth beneath the surface. Mackenzie *et al.* (2017) suggest a dip of $> 60°$ based on their observations of shortening. We also

recognize that steeper dips and a listric geometry are preferable to intermediate dips to drive uplift of the Papatea block. For these reasons, we infer that the preliminary fault dip range should be extended from known observations to cover a range of 55° ± 10° W. Further mapping and analysis of the slip vector and strike may be useful for developing a more robust dip range.

Character of the Papatea Fault and Subsidiary Fault Ruptures

The ~16-km-long north-northwest-striking west-dipping main strand of the Papatea fault is mapped almost continuously from ~3 km offshore of Waipapa Bay to George Stream in the north (Fig. 3a). The ~13-km-long but discontinuous western strand comprises the Okiwi, Wainui, back-basin, and Wharekiri rupture traces. The western strand is north to north-northwest trending and is typically subparallel to the main strand. At the bedrock scale, the main and western strands form an uplifted/extruded sliver of ~0.4–1.7 km width. Therefore, despite a lack of continuous surface rupture along the western strand, the Papatea fault is defined as a dual-stranded fault rupture. At the coast, a short minor (Edgecombe) strand occurs to the northeast of the main strand (Figs. 3a and 6). These strands are described from south to north. The Corner Hill, Waiautoa, and SCF faults are described in Ⓔ the electronic supplement.

Main Strand and Edgecombe Trace of the Papatea Fault

The Papatea fault is expressed offshore with oblique and partitioned displacement that evolves into a restraining termination to the south (Fig. 6; Cunningham and Mann, 2007, and references therein). Postearthquake bathymetry indicates that both strands exhibit clear vertical scarps on the seafloor uplifting a central horst block (Fig. 5 and Ⓔ Fig. S2; Clark *et al.*, 2017). Offshore, the main strand of the Papatea fault generally strikes north-northwest–south-southeast, but bends to the south-southwest toward its southern end (Fig. 6 and Ⓔ Fig. S1). The main strand is characterized offshore by up-to-the-west motion with scarps of up to 6 m height measured from profiles using EM2040 multibeam and green-band lidar over an aperture of ~200 m width (Figs. 5 and 6). This fault scarp is continuous as a single scarp from the coastline for ~1.8 km southward. From ~1 to 1.8 km offshore, scarp heights related to seafloor rupture vary between 3.5 ± 0.5 and 2.2 ± 0.2 m (Ⓔ Table S1 and Fig. S1). South of there, the main strand is characterized by a complex series of bends and stepovers for another ~2 km, ultimately terminating against the western strand. The southern termination of the main strand is characterized by a suite of northeast-striking link faults with both down-to-the-northwest and down-to-the-southeast vertical movements (Fig. 6). Vertical displacements on faults near its southern tip range from ~0.5 to 1.5 m. Several other discontinuous fault traces have been mapped outboard (southeast) of the stepover zone between the main and western strands. These are generally characterized by subtle up-to-the-northwest displacements at decimeter scale. No lateral displacements could be identified on the offshore traces of the Papatea fault, because they largely traverse rough bedrock seafloor with thin sediment drapes that provide few markers able to record lateral displacement. The southern end of the Papatea fault projects toward the northeastern offshore continuation of the Hope fault (Litchfield *et al.*, 2018). No continuous seafloor rupture or deformation of the seabed could be traced between the termination of the Papatea and Hope faults nor was any evidence of seafloor rupture observed on the Hope fault in this area from sub-bottom profiling.

Where the main strand of the Papatea fault comes onshore, the north-northwest-striking main strand is marked by an ~5.0 ± 0.4 m high scarp on the beach (Fig. 7d), after which it runs inland across sand dunes and through pine forest, where it displaces the South Island Main Trunk (SIMT) railway and State Highway 1 (SH1). The railway and SH1 were offset vertically ~4.0 ± 0.5 and 4.2 ± 0.2 m and left laterally ~3.9 ± 0.5 and 6.1 ± 0.5 m, respectively (Ⓔ Table S1). The main strand is expressed by a left-stepping mole track, turf rolls, and surface fractures and is followed inland to the steep northeast-facing coastal hillslopes. The Edgecombe strand occurs ~400 m to the northeast of the main strand and cuts across the coastal plain. This strand deformed SH1, producing a northeast-facing warp with down-to-the-northeast vertical separation of ~0.8 ± 0.2 m in the south and ~1.8 ± 0.4 m in the north in D-lidar profiles (Ⓔ Fig. S2). The Edgecombe strand was not observed across the beach or mapped offshore.

The main strand can be followed to the north across Tertiary hill country and Papatea Stream to the ~18 M m^3 Seafront landslide, one of the largest landslides that failed coseismically during the Kaikōura earthquake (Figs. 8 and 9a; Dellow *et al.*, 2017; Massey *et al.*, 2018). Here, the southeast-directed motion of the hanging wall is oblique (up to 45°) to the trend of the fault trace, resulting in approximately equal amounts of shortening and sinistral strike slip. Field and postearthquake lidar mapping indicate that where the rupture traverses the upper flanks of ridges in this area displacement is distributed across a fractured and bulged, fault-parallel, down-dip tapering, and locally fault-bounded deformation zone (e.g., trishear zone) that broadly follows the Amuri-Waima bedrock contact (Fig. 8). However, much of this portion of the main strand cannot be confidently mapped due to a lack of D-lidar coverage and due to failure and transport of the fault-zone downslope from the headscarp area as part of the very large landslides.

The 50-m-high headscarp of the Seafront landslide (Fig. 9a) broadly corresponds with the location of the main strand of the Papatea fault. Two faults in bedrock can be seen in the northern part of the exposed headscarp, the upper one within white Amuri Formation limestone, the lower one

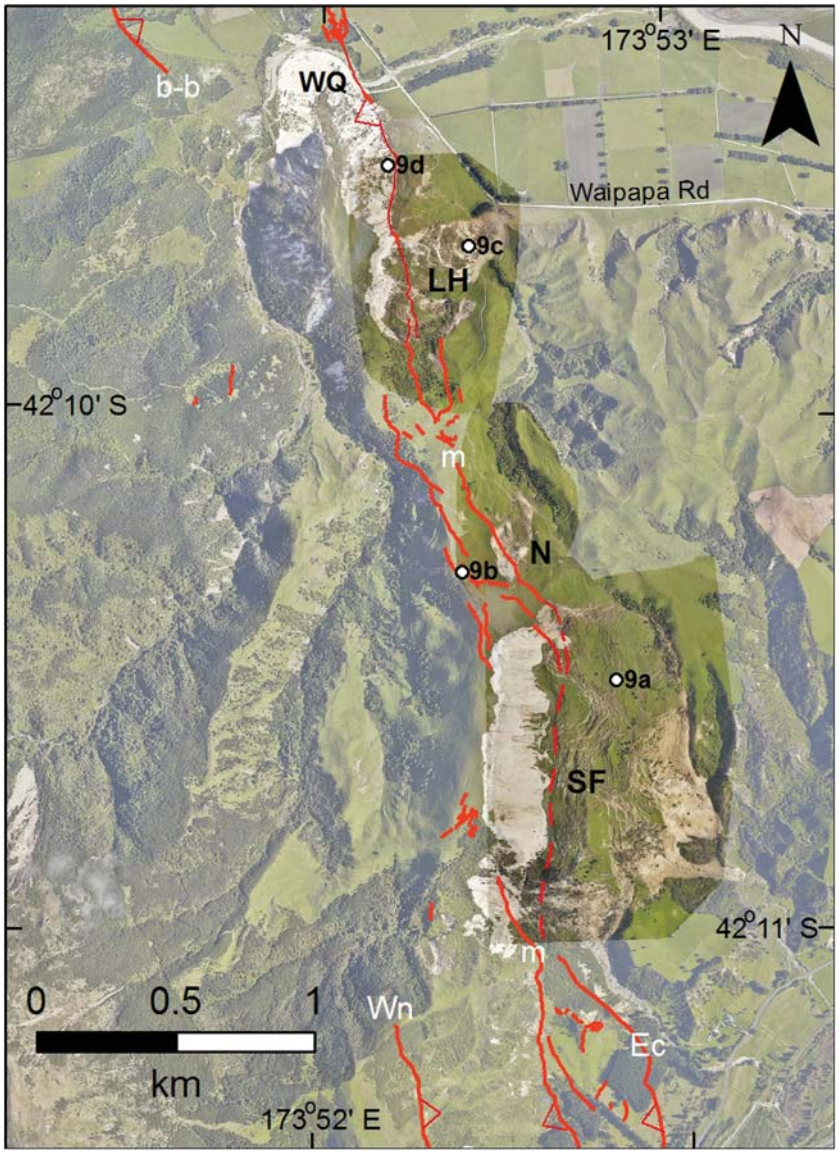

Figure 8. Detailed mapping at scale 1:5000 of the coastal hill country and landslide portions of the Papatea fault (main strand, m) shown on a postearthquake regional orthophoto, overlain by Unmanned Aerial Vehicle (UAV)-acquired orthophotos (darker) (the location is shown in Fig. 2b). Ec, Edgecombe; Wn, Wainui; b-b, back-basin. LH, Limestone Hills; N, Nelson; WQ, Waipapa Quarry; and SF, Seafront. Surface rupture is discontinuous or cryptic across these landslides and along much of the western strand (between b-b and Wn). The photo centers for Figure 9a–d are also shown.

juxtaposing white Amuri Formation limestone (Paleocene) over blue-gray siltstone or mudstone, inferred to be Waima Formation (Early Miocene). The lowermost fault coincides with the location of the base of a contractional bulge that is mapped north of the landslide, where an old fence is displaced up to 5 m sinistrally (e.g., Fig. 9b) across an 80-m-wide zone of deformation.

Further north, the main strand of the Papatea fault can be traced from the Seafront landslide, through the Nelson landslide, to the Limestone Hills landslide (Fig. 8; Massey *et al.*, 2018). Much of the ground surface deformation along this section of the fault is characterized by bulging and associated oversteepening of the hillslope. A farm track cut across the Nelson landslide provided access to the interior of the zone of bulging that shows that, in contrast to the thinly bedded white Amuri limestone outside the deformation zone, bedrock within the zone of bulging has been pulverized to fine angular gravel.

North-northwest-striking right-stepping en echelon fissures and faults bound the upslope and downslope margins of the deformation zone and cut across several saddles in more north-trending ridgelines. This disregard for topography, coupled with a common west-over-east transport direction (e.g., 2.4 m reverse slip at a rake of 45° NW on a fault oriented 134°/66° S), demonstrates a dominantly tectonic, not gravitational, origin for fractures and fissures along this stretch of the main strand. A fault zone is exposed in the northern wall of the Limestone Hills landslide headscarp (Fig. 9c) as a moderately-to-steeply west-dipping gouge-lined shear between white Amuri limestone to the west and light brown sheared limestone to the east.

North of the Limestone Hills landslide, the fault cuts obliquely across the eastern face of the limestone ridge (Fig. 9d), descending from ~160 to 60 m.a.s.l. to the floor of the Clarence Valley at the Waipapa Quarry. Across this slope, the D-lidar signal suggests a 4–5 m east-facing bulge, presumably created by east-vergent reverse motion. However, some caution is required for such an interpretation, because the postearthquake topography must have been thrust forward, as well as up, and this slope is host to many shallow landslides.

Surface rupture across the entrance road and stream bed at the Waipapa Quarry had been bulldozed before reconnaissance mapping began. North of there, fault ruptures typically strike northward toward Corner Hill and are characterized by two or more subparallel, or stepping, fault traces, often as a pair of frontal thrusts (Fig. 10). At the Papatea Pines site, vertical deformation (~7.7 ± 0.2 m up-to-the-west) occurs across a 160-m-wide zone, which is cut obliquely by sinistral reverse surface ruptures (Fig. 12c). A fenceline surveyed within the pines using a total station indicates ~4.8 ± 1.4 m of sinistral offset (Fig. 10; Ⓔ Table S1). The frontal traces cross Waipapa Road and form a series of overlapping thrusts, whereas a secondary distributed parallel fault zone runs underneath a nearby house that was removed

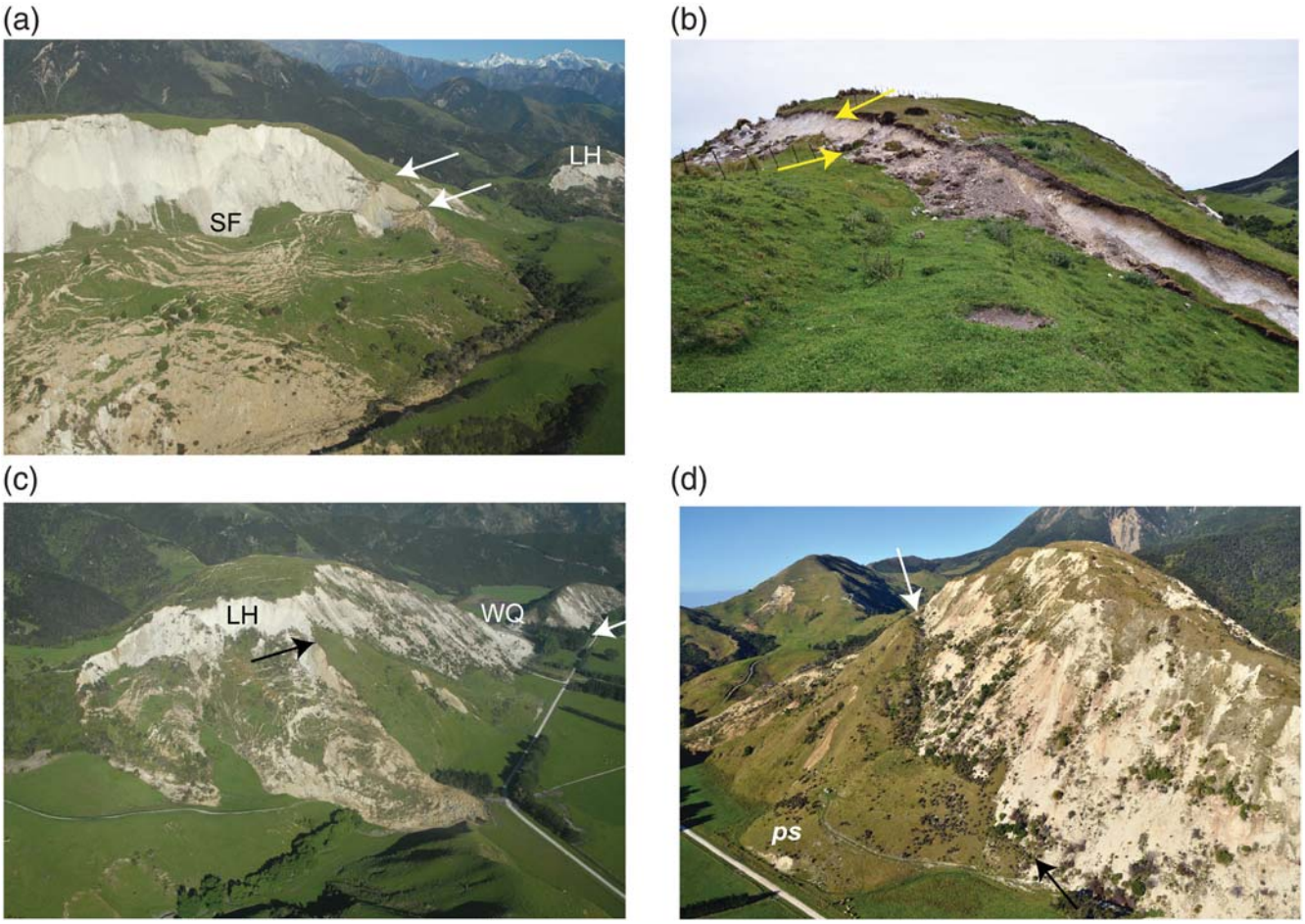

Figure 9. Photographs from the hill country portion of the Papatea fault (locations are shown in Fig. 8). (a) Aerial view of the northern end of the Seafront (SF) landslide, white arrows mark the upper and lower margins of the fault-zone trishear wedge. (b) A scarp that crosses over the back of the Papatea escarpment drainage divide and is thus considered to be tectonic in origin; yellow arrows mark the base of a fenceline that is offset sinistrally. (c) Aerial view of the Limestone Hills (LH) landslide. The Papatea fault cuts obliquely across this hillslope, shown by a black arrow where the bedrock relationship is intact. (d) View to the south looking along the main strand of the fault (denoted by arrows) immediately south of the WQ; ps indicates a paleolandslide deposit at the toe of the slope.

due to damage from ground-surface faulting and deformation (Van Dissen *et al.*, 2018).

Between Waipapa Quarry and the Clarence River, the main strand of the fault is expressed by surface ruptures immediately east of the homestead of Middle Hill Station (MHS). In this area, two broad alluvial terrace remnants are preserved on the western upthrown side of the fault. These terraces, T1 and T2 (Fig. 10), are ~30 ± 2 and ~18 ± 2 m, respectively, above the younger terrace preserved to the east of the fault (on pre-earthquake lidar). The high scarps along this stretch of the fault are bordered at their eastern edge by a reverse-fault trace, typically with one or more additional inboard reverse-fault traces (Figs. 10 and 11). The maximum coseismic vertical throw measured from D-lidar (9.5 ± 0.5 m) occurred near the MHS homestead. Toward the Clarence River, throw in excess of 9 m is recorded, in association with a north-striking (005°) stretch of the fault for ~500 m. As the fault traces bends to east of north, the broad fault scarp includes a stepping zone of north-trending normal rupture traces that form narrow grabens on the hanging wall (Fig. 12a). Scarp profiles in D-lidar here are distinctly rounded; that is, they have an oversteepened front consistent with reverse motion and shortening with extension occurring near the scarp crest. The average sinistral offset measured across a farm road and an adjacent fenceline at MHS is ~4.3 ± 0.4 m (Ⓔ Table S1). Oral accounts stated that there was no slope or pre-existing scarp across the extension of Waipapa Road to Wharekiri Stream prior to the earthquake; this was confirmed by D-lidar profiles that indicate ~8–9 m of coseismic vertical throw there (Figs. 11b and 12c). At the Clarence River, white Amuri Formation limestone on the hanging-wall side of the fault was uplifted by ~8 m relative to the footwall. This uplift has resulted in the formation of rapids and a narrow gorge in the limestone now exposed in the river bed upstream from the fault (Fig. 11d) where the river has down-cut to re-establish its gradient across the fault zone. Miller and Wharekiri streams merge with the Clarence River near its intersection

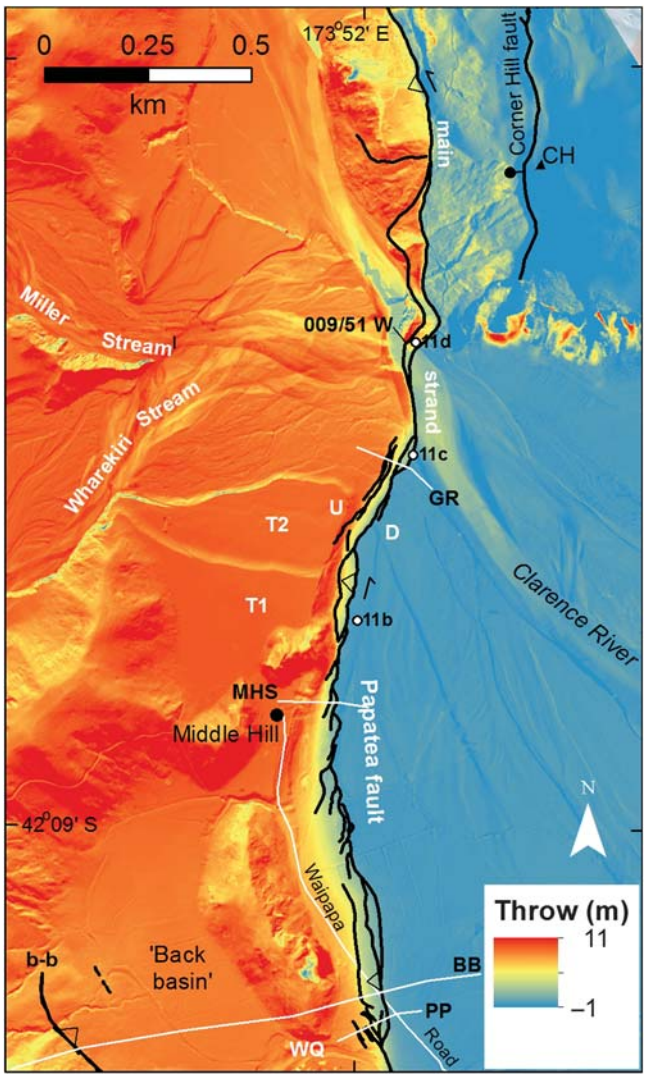

Figure 10. Detailed mapping at scale 1:5000 of the main strand of the Papatea fault (black lines) in the Middle Hill Station (MHS) area shown on a vertical D-lidar map highlighting the exceptional throw across the fault (the locations are shown in Fig. 2b). Corner Hill (CH), fault attitude, and two prominent uplifted alluvial surfaces (T1 and T2) are also shown. Photo centers for Figure 11a–d are also shown. Three profiles at Papatea Pines (PP), MHS, and grabens (GR) are shown in Figure 12. Profile BB is shown in Ⓔ Figure S2.

with the fault, and they have also entrenched to re-grade to the new level of the river (Figs. 10 and 11c).

The main strand of the Papatea fault is exposed in bedrock on the true left bank of the Clarence River, below Corner Hill, where it has two subparallel rupture traces (Fig. 10). The trace closest to the river juxtaposes Amuri limestone against a ~1 m wide sheared zone of cataclasite with an attitude of 009°/51° W (Fig. 11d). Slickenlines plunge steeply (~50°) at this locality. Immediately east of this fault zone, the lithology is an unconsolidated dark green, gritty sandstone of uncertain origin, and the eastern trace is poorly exposed. The expression of the fault in bedrock here is consistent with interpretations based on exposures in the Seafront and Limestone Hills landslides that indicate a fault-zone wedge. The two traces cross topography with scarps that follow pre-existing saddles below Corner Hill and thrust topography upslope to the east. Fencelines and farm tracks in this area indicate sinistral horizontal offsets of ~1–1.6 m on the western trace and up to 6 m on the eastern trace (Ⓔ Table S1). The two traces appear to merge ~300 m west of Corner Hill. North of there, the fault forms a large east-vergent reverse scarp that overthrusts topography along a fault-parallel trough.

From north of Corner Hill to the collapsed Glen Alton bridge (Fig. 13), the main trace of the Papatea fault occurs within the bed of the Clarence River. In this area, the river has avulsed into the structural depression on the eastern (downthrown) side of the fault and formed a temporary lake near Corner Hill, referred to here as Lake Murray (Fig. 13). Over this 3-km stretch, the fault rupture zone changes strike twice to bend from north to northwest strikes. In the south, the fault trace is defined by the large scarps that formed the western edge of Lake Murray immediately north of Corner Hill (Fig. 14a). For ~0.5 km north of the overflow of the lake, the fault is characterized by a series of arcuate frontal reverse-fault traces with an average strike of 315° and secondary (dip-slip) traces that strike 330° and form a 20–40-m-wide zone of faulting. Field estimates of the scarp height in this area are at least 4–6 m up-to-the-west, though some of the scarp relief is certainly concealed underwater in the lake, because far-field D-lidar profiles indicate ~7–8 m of throw.

For the next ~1.4 km, the ~325°-trending main trace fault formed the margin of Lake Murray, typified by a large scarp with throw of ~7.0 ± 0.5 m formed across a width of ~10 m (Fig. 13). In the middle part of this section, the zone of deformation is at least 40–60 m wide and is characterized by a frontal reverse-fault scarp, secondary reverse (or dip-slip scarp), and southwest-facing scarps that are interpreted as backthrusts. Near the northern end of this stretch, a major pre-existing overflow channel of the Clarence River now flows across the fault and has eroded the scarp (Fig. 14b). North of this channel, the land is more intensively farmed and there are several fencelines that intersect the fault at a high angle. The southernmost of these fencelines has a sinistral offset of ~4.3 ± 0.5 m, in association with a scarp height of ~7.5 ± 0.5 m assessed from D-lidar (Ⓔ Table S1).

Further to the north, the fault crosses what is locally known as Priam's Flat where it changes strike, being characterized there by a frontal reverse-fault trace with strike ~305° along which the avulsed Clarence River flows (Fig. 13). This stretch of the main strand is typified by a large scarp with a height of 6.5 ± 0.5 m and by a series of parallel en echelon tears in the hanging-wall side of the scarp. These tears are typically 90–120 m long and have an average strike of 290° (Figs. 14c,d). The tears are consistently 15–25 m apart and define a deformation zone of 30–50 m width, though distributed warping can be detected in profiles beyond this width. The change from fault-parallel structures in the south to en echelon tears in the north is consistent with

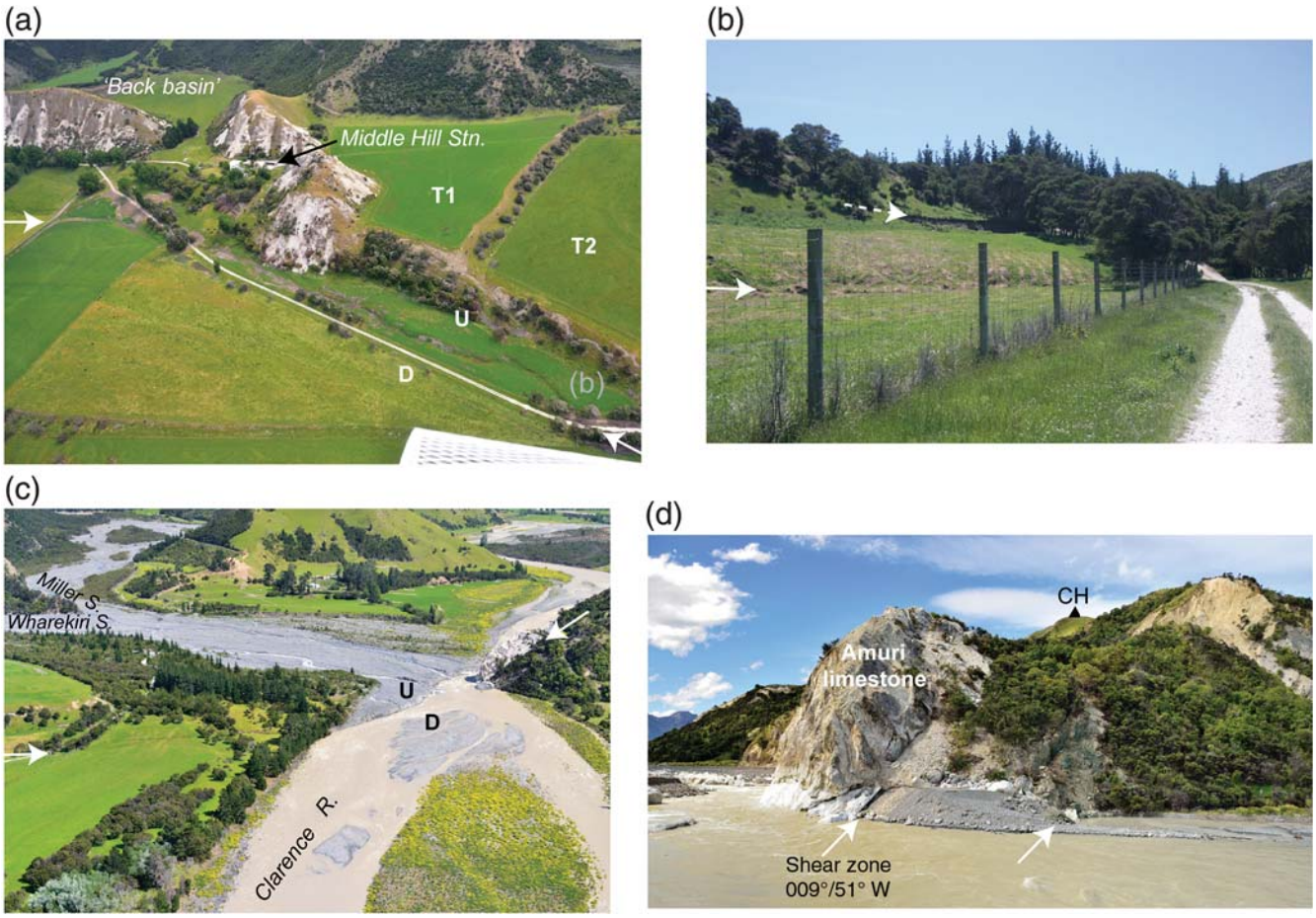

Figure 11. Photographs from the MHS to Corner Hill portion of the Papatea fault (locations are shown in Fig. 10). (a) Oblique aerial view of northern extension of Waipapa Road at MHS. White arrows mark the sinuous frontal reverse-fault scarp. T1 and T2 are uplifted and preserved alluvial surfaces. (b) Coseismic frontal reverse-fault scarp marked by solid arrow. Dashed arrow marks the upper edge of a crestal graben. The bending white limestone gravel road was flat before the earthquake. (c) Oblique aerial view of the confluence of Miller and Wharekiri streams with the Clarence River. The streams catchments were uplifted ~8 m on the northwest side of the fault, forming an abrupt scarp (between white arrows and U, D). (d) View looking north showing the Papatea fault (zone) on the north side of the Clarence River near Corner Hill (CH). Arrows mark the location of two distinct dipping fault zones. Note the uplift of Amuri limestone bedrock on the upthrown (left) side of the fault zone adjacent to river and uplift of alluvial gravel between the two traces.

the observed 20° strike change from Lake Murray to Priam's Flat. A fenceline along this stretch was offset sinistrally by ~4.4 ± 0.5 m. Two other sinistral offsets of ~2 m were measured along this stretch; however, these are probably minimum values because the markers do not fully extend across the rupture zone. The northwestern end of this stretch (south of the Glen Alton bridge) is defined by a northwest-trending fault scarp across an active river bar, around which the river split and avulsed following the earthquake (Fig. 14c). With time following the earthquake, the Clarence River has continued to modify the geomorphology of Priam's Flat, and the overflow sill of Lake Murray has been eroded through, causing evacuation of the lake.

Northwest of Glen Alton bridge, the main strand of the Papatea fault occurs as a branching zone of distributed deformation that widens to the northwest (Fig. 15). The frontal (northernmost) trace of the fault is a continuation of the scarp observed on the true left side of the Clarence River, that is, a large northwest-trending (315°) scarp, mapped as a sinuous trace on lidar. From the river, the frontal trace has a broad rounded fault scarp of 1.5–2.5 m total height. It crosses Clarence Valley Road just east of a house named Harkaway Villa (Fig. 16a). This discrete scarp was measured at the road with height ~1 m and with no apparent horizontal offset. However, the vertical throw across the width of the distributed fault zone measured using D-lidar is as much as 5 m here. The large scarp continues to the northwest and increases to ~4 m height as the frontal trace diverges farther from the secondary splays of the fault. This trace crosses Waipapa Road adjacent to a formerly level cattle corral, now deformed by faulting and bulging within the scarp. The road here displays discrete offsets of ~1 m vertical and ~1 m sinistral. The frontal trace is mapped as far as George Stream (the edge of D-lidar coverage), after which it cannot be located in the

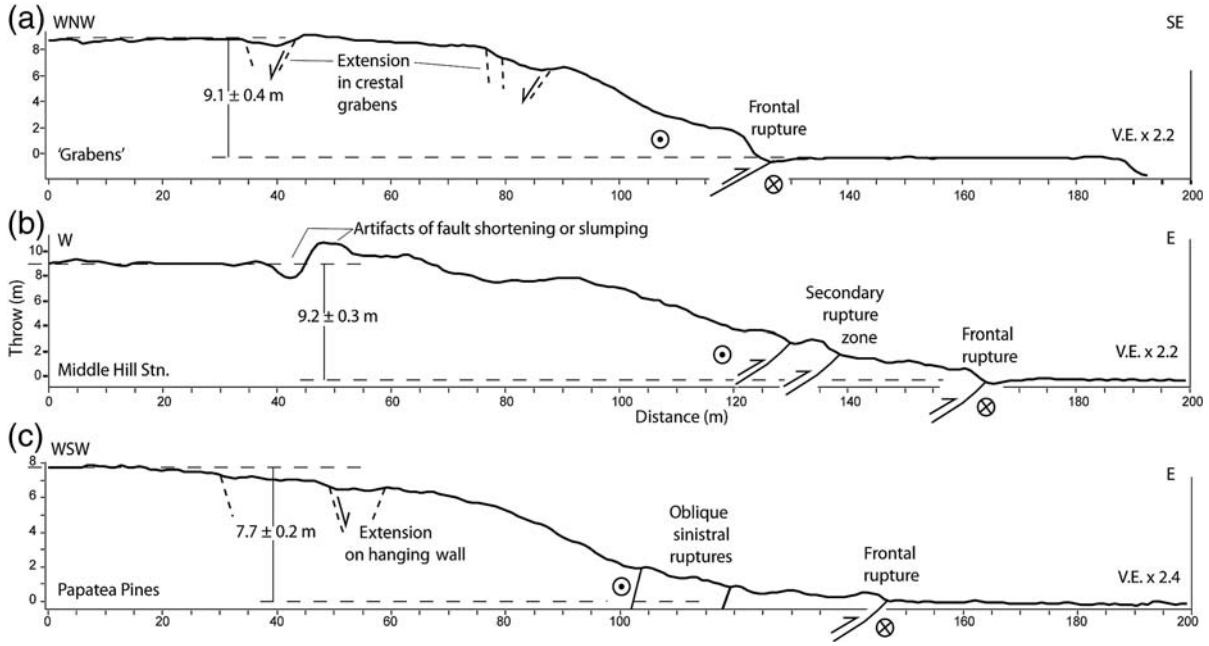

Figure 12. Uncorrected D-lidar profiles across the main strand of the Papatea fault at three locations in the MHS area (a) Grabens; (b) MHS; (c) Papatea Pines sites (see Fig. 10 for locations). The vertical throw (*y* axis) in these areas is large, and fault deformation occurs over widths of > 100 m. Fault dips are for schematic purposes only.

field or on postearthquake lidar, possibly due to it dying out to the west or because the trace is parallel to channels on the fan associated with George Stream. Upstream of this trace, on the floodplain of George Stream, three short rupture traces with trends orthogonal to the Papatea fault (020°–030°) were observed in lidar datasets and confirmed in the field, having ~0.8 m down-to-the-east throw (Fig. 15). Whereas no discrete offsets have been identified further up George Stream from here, we observed outcrops with faulted deposits of likely late Quaternary age and rocks related to a wider zone of bedrock shear in the true right valley wall of George Stream. Though no surface ruptures have been documented within 1.8 km of the Jordan thrust fault, these observations lead us to infer that the main strand of the Papatea fault continues to the northwest up George Stream (Fig. 15).

Secondary splays of the main strand diverge from the frontal scarp at the Clarence River. These splays form a discrete west-northwest-trending (~290°) zone that extends across alluvial terraces for more than 400 m to Waiautoa Road (Fig. 15). The zone comprises a series of arcuate-to-stepping tensional fractures that account for ~3 m of vertical offset in the southeast, diminishing to ~1 m in the northwest, similar to the main trace of the fault. This secondary zone crosses a field with rows of recently planted fruit trees (Fig. 16a). RTK-GPS surveying of these six orchard rows yields an average sinistral offset of 4.5 ± 0.4 m with discrete sinistral offset and warping observed across the entire width of the fault zone. The secondary zone becomes focused into a pair of traces where it crosses Clarence Valley Road. From there it proceeds through a house and yard to Waiautoa Road where ~0.25 m throw and ~0.1 m sinistral offset were measured during reconnaissance. D-lidar indicates up to ~1.2 m vertical throw at this location.

The character of faulting on the secondary fault zone changes to the west of Waiautoa Road as it climbs into hill country underlain by Mid Cretaceous sandstones that abut the Papatea fault at the northern tip of the Puhipuhi Syncline (Fig. 4). This zone widens from ~90 to 120 m across a preserved high surface on the hanging wall of the Papatea fault where the Millard house is sited (Fig. 16c). These traces are typically sinuous and are characterized by tensional gashes and openings. Overall, this zone takes the appearance of a large gravitational feature; however, this secondary zone is considered as an active zone of oblique extensional tectonic deformation in the hanging wall of the Papatea fault, rather than as a landslide.

Western Strand of the Papatea Fault

Offshore of Waipapa Bay, the north-striking western strand is near continuous for ~3.8 km and is characterized by up-to-the-east motion with scarp heights of up to ~4.4 ± 0.4 m (Fig. 6). At its southern end, the Okiwi trace displays a slightly sinuous trace with decimeter-scale scarps formed on the seafloor. About 1 km south of the pre-existing shore platform, this trace steps left (to the Wainui trace) by ~140 m to the east and proceeds to the shore platform, uplifting bedrock in an up-to-the-east fashion. The Wainui trace juxtaposes Amuri limestone (to the west) against Waima siltstone in the shore platform. Southwest of the Papatea fault, coseismic rupture on the Paparoa Point fault was recognized across

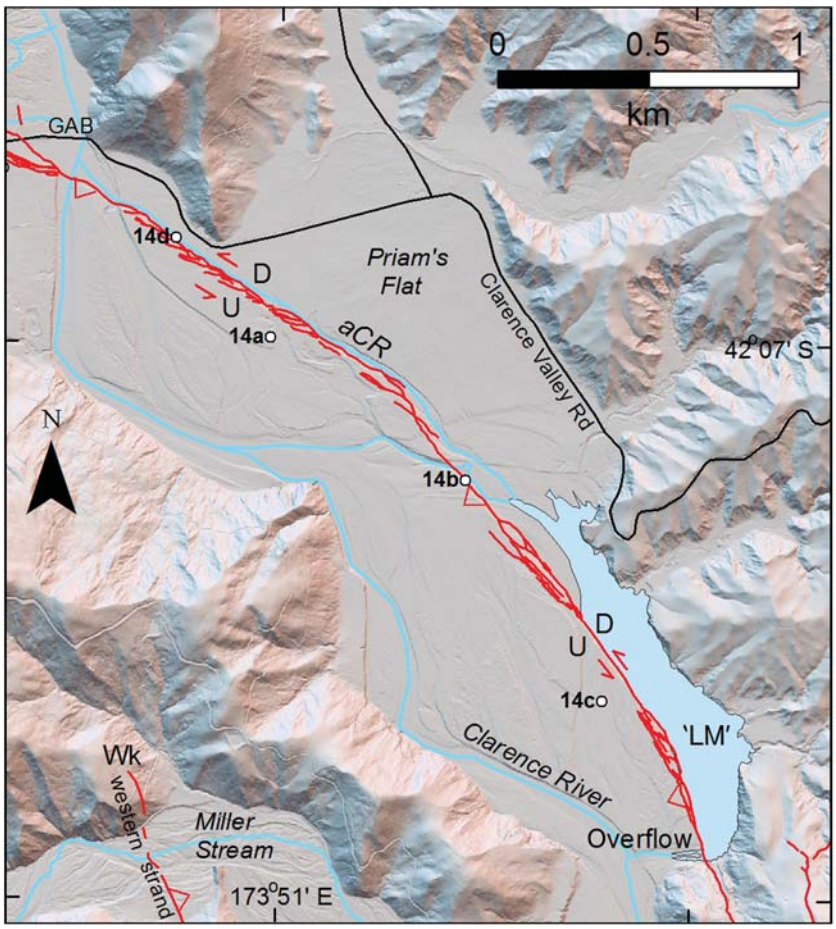

Figure 13. Detailed mapping at scale 1:5000 of the main strand of the Papatea fault in the Priam's Flat area shown on postearthquake lidar hillshade model (the location is shown in Fig. 2b). Northern end of the western strand/Wharekiri trace (Wk) of the Papatea fault is also shown. Photo centers are also shown for Figure 14a–d, highlighting two major changes in trend along Lake Murray (LM) and the avulsed Clarence River (aCR). Persistent river avulsion has resulted in the erosion of the approach to the Glen Alton bridge (GAB) and the evacuation of Lake Murray.

slopes and beach deposits at the coast (Fig. 3; Clark *et al.*, 2017; Litchfield *et al.*, 2018).

The Wainui trace and main strand of the fault are ~800 m apart where they cut the coastline. The Wainui trace is dramatically expressed at the coastline by a sharp scarp and significant uplift that displaces the shore platform and exposes a shear zone in the bedrock (Fig. 7). The SIMT railway and SH1 are offset by ~3.0 ± 0.2 and ~2.8 ± 0.4 m down-to-the-west, respectively (Figs. 6 and 7c). Measured strike slip across storm beach ridges, the SIMT, and SH1 appears to be small (i.e., < 1 m). The vertical throw across beach deposits is ~3.0 ± 0.4 m, and the scarp across the bedrock shore platform varies between ~1.2 ± 0.5 and 1.7 ± 0.4 m in height. Uplift of displaced intertidal biota was estimated at 4.4 ± 0.25 m on the upthrown side of the western strand and 1.8 ± 0.13 m on the downthrown side (Clark *et al.*, 2017). A 2.5-km-long D-lidar profile drawn along SH1 indicates ~2.2 m of up-to-the-west total far-field uplift across all three strands of the Papatea fault at the coast (Ⓔ Fig. S2).

Aerial imagery indicates that Waima Formation siltstone exposed in the uplifted shore platform consistently strikes at ~145°–155° and is crosscut by the western strand. At the coast, a shear zone is exposed on the near-vertical fault plane (Fig. 7b). The average of eight strike and dip attitudes on the exposed fault surface at this location is 168°/84° W. The fault-plane surface has at least two prominent sets of slickenside striations. The most common set is an oblique and weathered set of wear lines that indicate normal sinistral motion (seven rake measurements from 25°–41° S; average 32° S). In contrast, a second set is characterized by grooves in the surficial clay gouge (possibly formed by pebbles gouging along the slip surface) that indicates motion in the dip direction (Ⓔ Fig. S3; four rake measurements from 78° S to 81° N; average rake 90°). Lensen (1962) records a bedding dip of 80° E in the shore platform at this locality. Based on the offset of linear piercing lines (SH1, SIMT, and beach berms), we interpret the latter set of slickenline grooves as being those that relate to slip in the 2016 earthquake, whereas the former probably relate to an earlier phase of fault movement. In addition, based on bedding dips, in places an overhanging rupture plane (Ⓔ Fig. S3) and the deformation of the horst block between the Wainui and main strands (Lensen, 1962; Clark *et al.*, 2017), we surmise that the fault plane related to the western strand is essentially vertical and probably joins the main strand of the fault at depth (Ⓔ Fig. S2). Such structures have been observed on other recent reverse-fault ruptures (Yu *et al.*, 2010) and are consistent with the observation of a kilometer-scale bedrock sliver along the fault.

In the hill country above the coastal platform, the western and main strands are < 400 m apart (Fig. 6). From the highway, the Wainui trace of the western strand can be followed for ~800 m northward, traversing low hummocky terrain in which the fault scarp is still obvious. Further to the north, the fault scarp traverses across the east-facing hillslopes above Waipapa Bay and becomes less distinct within the steeper topography. On land, vertical displacement measured from D-lidar profiles is typified by down-to-the-west scarps that diminish from ~3 m height at the coast to 0–1.5 m high ~1 km inland. Fault traces are incompletely mapped to the north, not only due to a lack of D-lidar coverage, but also due to a lack of conspicuous fault rupture expression. Our current interpretation is that the western strand is a fault that lacks recognizable surface rupture

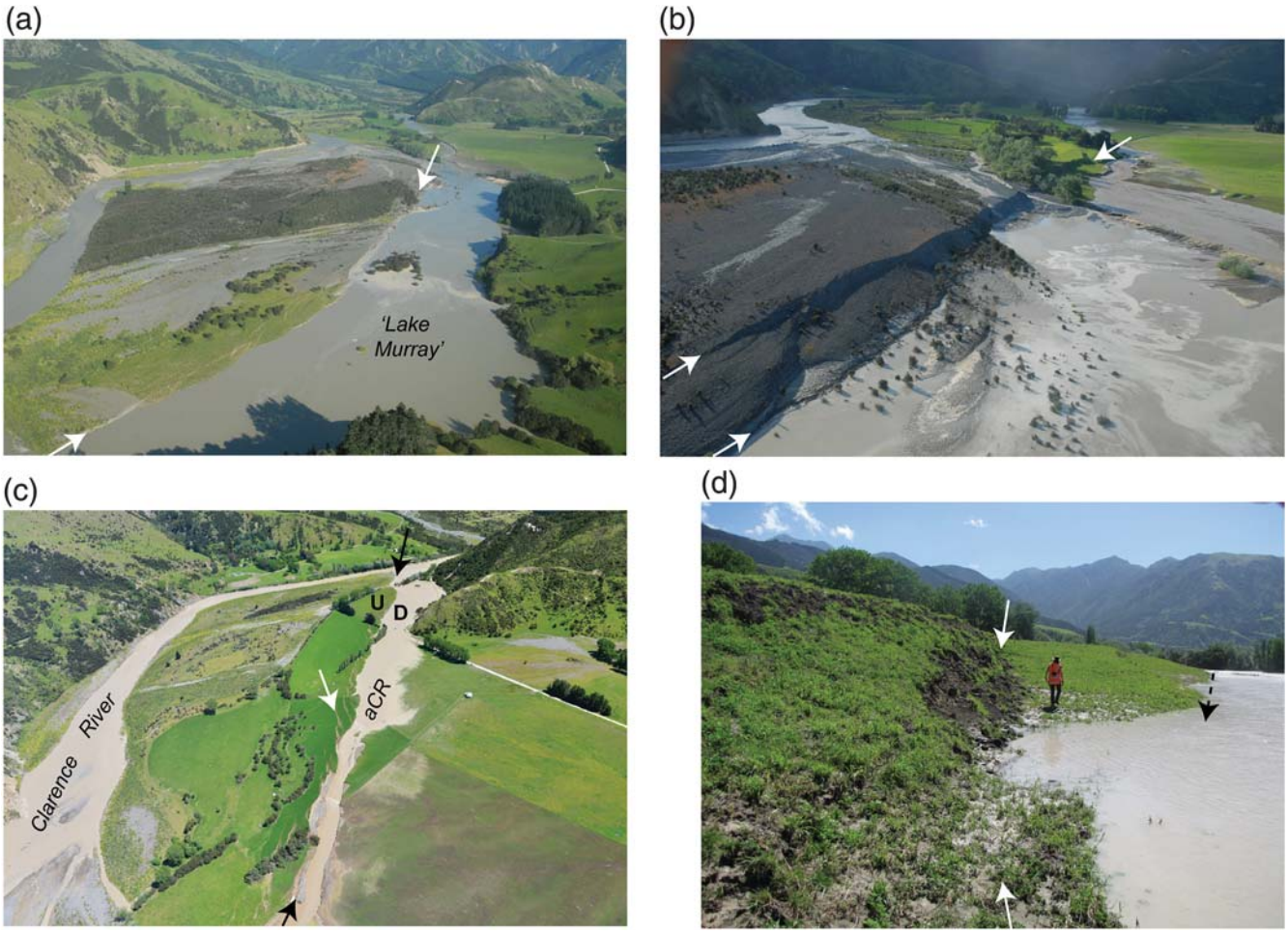

Figure 14. Photographs from the avulsed Clarence River portion of the Papatea fault (locations are shown in Fig. 13). (a) View along Lake Murray where the trend of the rupture zone changes from 320°–330° to about 340°–345° in the south. (b) South of Priam's Flat the fault rupture is characterized by overlapping reverse-fault traces and antithetic back-thrust traces. The throw here is about 7.5 ± 0.5 m. (c) Oblique aerial view of avulsed river where the average fault strike is about 310° (between black arrows) and the hanging wall is characterized by en echelon tear faults (indicated by white arrow). (d) En echelon tear faults (marked by white arrows) running oblique to the main fault scarp trend (indicated by course of the river and dashed arrow). Person for scale.

between the back of the Seafront landslide and the back-basin trace. However, because of the complex nature of the faulting along the range front and disruption of the key geologic relationships due to landsliding, the structure and rupture pattern of the Papatea fault in this area is equivocal.

The back-basin trace refers to an area west of MHS where a large basin exists behind the prominent Amuri limestone hills. Discontinuous surface rupture has been located at the western edge of this basin on trend with the Wainui and Wharekiri traces. Some ruptures show down-to-the-east warping and cracking, whereas on D-lidar there appears to be down-to-the-west motion at the hillslope edge (Ⓔ Fig. S3).

Analysis of D-lidar enabled the recognition of another trace of the western strand in the hills west of the main strand, crossing Wharekiri and Miller streams (Fig. 3b and Ⓔ Fig. S4). The Wharekiri trace is a north-northwest-trending (340°) fault trace associated with a down-to-the-west step in topography. This trace is mapped for ~2 km between Wharekiri and Miller streams with typical vertical throw of 1–2 m. Postearthquake mapping and imagery indicates surface cracking and rupture across open ground and a farm track. In places, surface rupture is associated with pre-existing and uphill-facing topography. A fenceline crossing the Wharekiri trace at its highest point showed no lateral offset. The very straight fault trace crosscutting topography implies that the Wharekiri trace has a steep fault dip at the surface (Ⓔ Fig. S3). Because of its straightness compared with the main strand (Fig. 2), the distance between the two strands varies from ~1 to 1.7 km across strike. Adjacent to both streams, the Wharekiri trace is found in association with the back edge of high alluvial terraces. These older terraces are likely preserved by uplift within the fault zone of the Papatea fault.

The along-strike deformation from the Wainui to back-basin and Wharekiri traces supports the wider tectonic geomorphology that defines a tectonic sliver between the

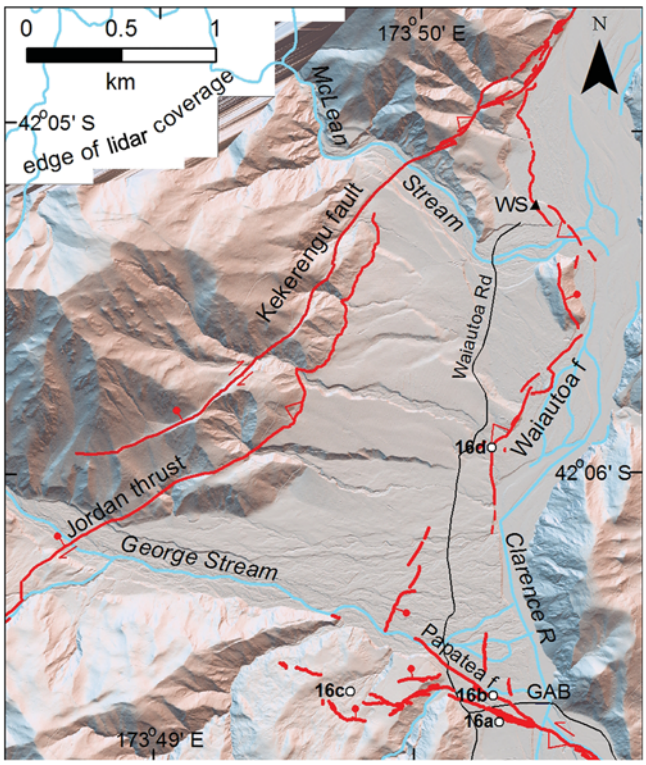

Figure 15. Detailed fault mapping at scale 1:5000 of the northwestern end of the Papatea fault near George Stream and including mapping of the Jordan thrust, Kekerengu and Waiautoa faults (the location is shown in Fig. 2b). Teeth symbols mark the hanging-wall side of reverse/thrust ruptures; bar and ball symbols mark normal or unknown dip-slip motion. Surface rupture on the Papatea fault terminates within George Stream but projects toward the Jordan thrust. Photo centers for Figure 16a–d are also shown. WS, Waiautoa station; GAB, Glen Alton bridge.

main and western strands that partitions strain along its length (Fig. 3 and Ⓔ Fig. S3). Collectively, these data lead us to infer that the western strand dips near vertical and is part of the wider Papatea fault zone.

Coseismic Offset Distribution and Slip Calculations

Preliminary distributions of throw and strike-slip measurements are presented in Figure 17 from various methods. The distribution of coseismic throw measurements is near continuous, due in large part to the availability of D-lidar. In contrast, however, there is considerable uncertainty in the sinistral offset distribution and a lack of data for the shortening and dip components of our analyses. Nevertheless, we infer that individual and combined measurements are sufficient to develop a preliminary ground-surface displacement dataset for the Papatea fault from which a maximum slip calculation can be made. At one locality where the fault dip is evident (the Clarence River outcrop), a net slip calculation can be made. Figure 17a highlights the strike range of the fault that has been presented as a companion tool to the offset distributions.

Vertical Throw

The oblique-slip Papatea fault has a dominantly reverse style of movement consistent with uplift of the Papatea block on a west-dipping structure. The maximum throw measured across the main strand of the fault is near MHS ($\sim$9.5 $\pm$ 0.5 m), and throw is consistently $\geq$ 6 m over a distance of 5–6 km, centered around the intersection with the Clarence River at Corner Hill (Figs. 12 and 17b). At the coast, the main strand displays $\sim$5.0 $\pm$ 0.4 m vertical throw. A secondary peak in throw (up to 6–7 m) occurs $\sim$200–500 m offshore that diminishes toward zero $\sim$4 km offshore of Waipapa Bay. Throw across the Seafront to Limestone Hills landslide area is difficult to assess but is inferred from field measurements to be several meters. North of Corner Hill, throw diminishes from 7–8 m to $\sim$5.5 m at Glen Alton bridge, after which it falls to 3 m or less on the true right side of the Clarence River. Vertical throw for the frontal trace of the main strand could not be assessed beyond its mapped termination at George Stream; therefore, we taper the throw to zero toward the Jordan thrust. The calculated average throw for the main strand is $\sim$5.1 $\pm$ 0.2 m. North of Glen Alton bridge, $\sim$1 m of vertical throw may in part be transferred from the Papatea fault to the east-verging reverse-slip Waiautoa fault (Fig. 17b; Langridge *et al.*, 2017).

The western strand of the Papatea fault generally displays up-to-the-east throw across steeply dipping faults. Throws on the western strand are shown as negative values in Figure 17c because we regard positive throw as up-to-the-west, sympathetic with the main strand. Near and just offshore of the coast, the Wainui trace displays up to $\sim$3.0 $\pm$ 0.5 m throw that diminishes to the north to zero by $\sim$1.2 km inland. The Wharekiri trace displays a peak throw of $\sim$2 m assessed from vertical offsets on D-lidar profiles between Wharekiri and Miller streams.

Strike Slip

The strike-slip component of motion on the main strand of the Papatea fault was measured onshore from offsets of cultural features, including fencelines, ditches, roads, and railway lines (Ⓔ Table S1; Fig. 17d). All measured horizontal offsets were sinistral; the peak offset is $\sim$6.1 $\pm$ 0.5 m measured from the offset railway line across the main strand of the fault near the coast. Sinistral offsets have not been recognized on the offshore parts of the fault zone, due to a lack of lateral offset markers; therefore, our sinistral slip profile diminishes toward zero offshore to the south. Many of the sinistral offsets are considered to be minimum values. The most reliable measurements indicate a consistent 4–6 m of sinistral offset along the length of the fault (Fig. 17d). As with throw, sinistral offsets diminish to the northwest of Glen Alton bridge and cannot be assessed within George Stream. We find little evidence for measurable strike slip on the western strand of the fault.

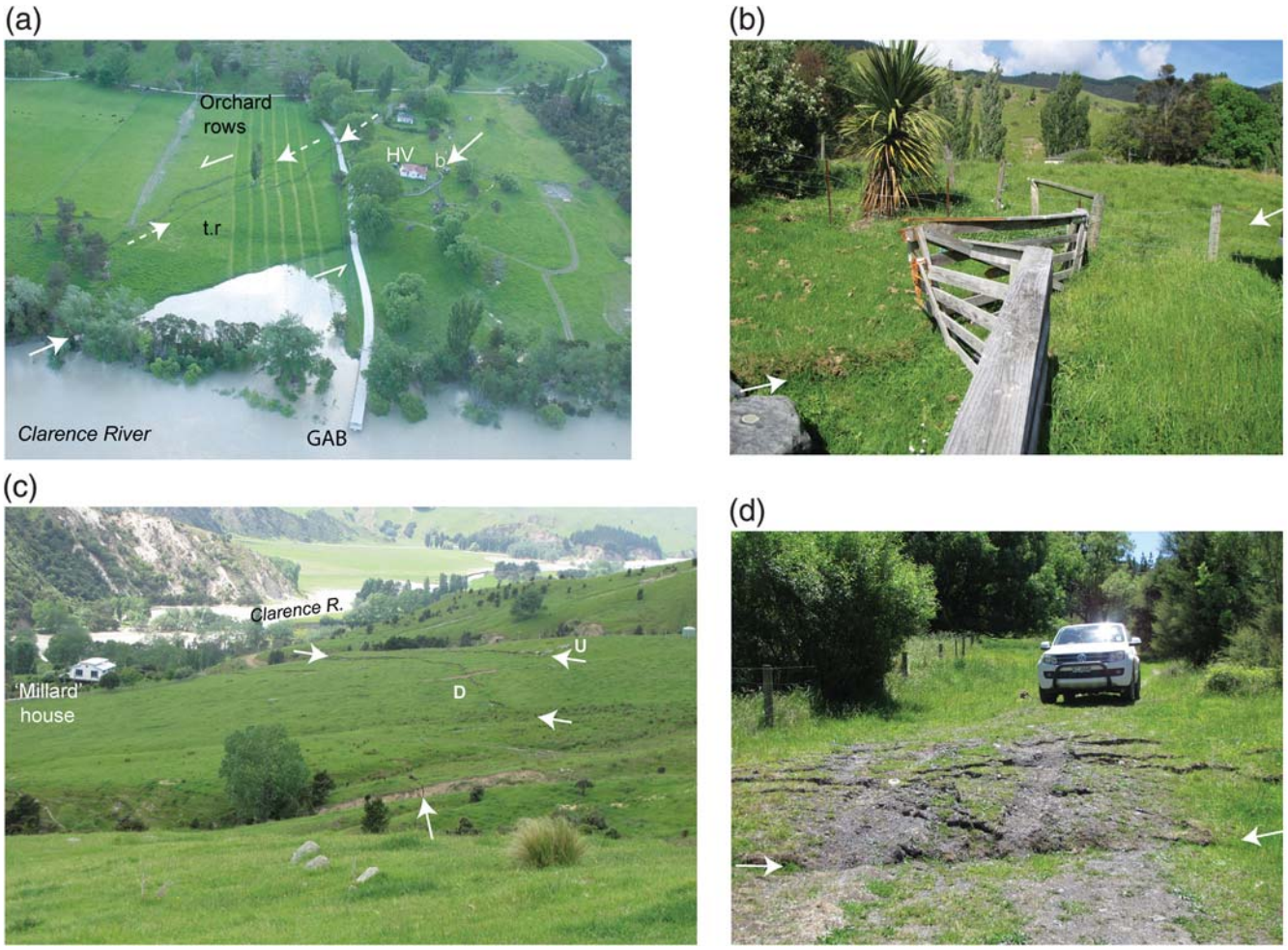

Figure 16. Photographs from the northwestern end of the Papatea fault and Waiautoa fault (locations are shown in Fig. 15). (a) Oblique aerial view of the distributed zone of surface deformation on the true right side of the Clarence River. Horizontal offsets were measured from a set of six fruit tree rows producing an average of 4.5 ± 0.4 m sinistral. GAB, Glen Alton bridge; HV, Harkaway Villa; t.r, river terrace riser. (b) Wooden gate offset by the frontal trace of the Papatea fault (at HV; between white arrows) with both sinistral and vertical offset. The gate is left laterally offset and shortened, as is the fenceline. (c) The pattern of distributed faulting observed in the hanging wall of the Papatea fault, indicated by sinuous scarps and open cracks (white arrows). (d) Small Waiautoa fault thrust scarp (denoted by white arrows) with ~0.4 m throw.

Maximum Coseismic Surface Slip on the Papatea Fault

The maximum coseismic surface slip on the sinistral reverse main strand of the Papatea fault comes from a combination of the maximum throw (~9.5 m at MHS) and a nearby sinistral offset observation (4.3 ± 0.5 m). Combined with the inferred fault dip of 55 ± 10° W, we calculate a maximum slip value of ~12 ± 2 m. The uncertainty range comes from combining the maximum throw on a 65° W-dipping fault plane and no strike slip (the low end of the range) versus the maximum throw on a 45° dipping fault plane with the maximum sinistral offset (the high end of the range).

A 2 km stretch of the main strand between Middle Hill and Corner Hill exhibits throws in excess of 8 m. These throws occur in association with the north- to north-northeast-striking stretch of the fault, where the relative block motions promote a larger vertical component of motion. In addition, we are more confident of the fault dip (~51° W) in this area than elsewhere, which is evidence to support the upper end of the maximum displacement range. Some of the highest sinistral offsets appear to be associated with north-northwest-striking stretches of the fault that may therefore be predisposed to having a larger horizontal component of slip.

The maximum surface slip value for the entire Papatea fault comes from the main strand, less the surface slip on the western strands. We measure ~0.5 m average throw (down-to-the-west) on the Wharekiri trace across strike from MHS. If we assume mainly dip-slip motion on this trace (as also observed on the Wainui trace at the coast), then the average slip must be ~0.5 m there. Thus, the maximum net oblique (sinistral reverse) surface slip for the Papatea fault assessed across the main and western strands at MHS is ~11.5 ± 2 m.

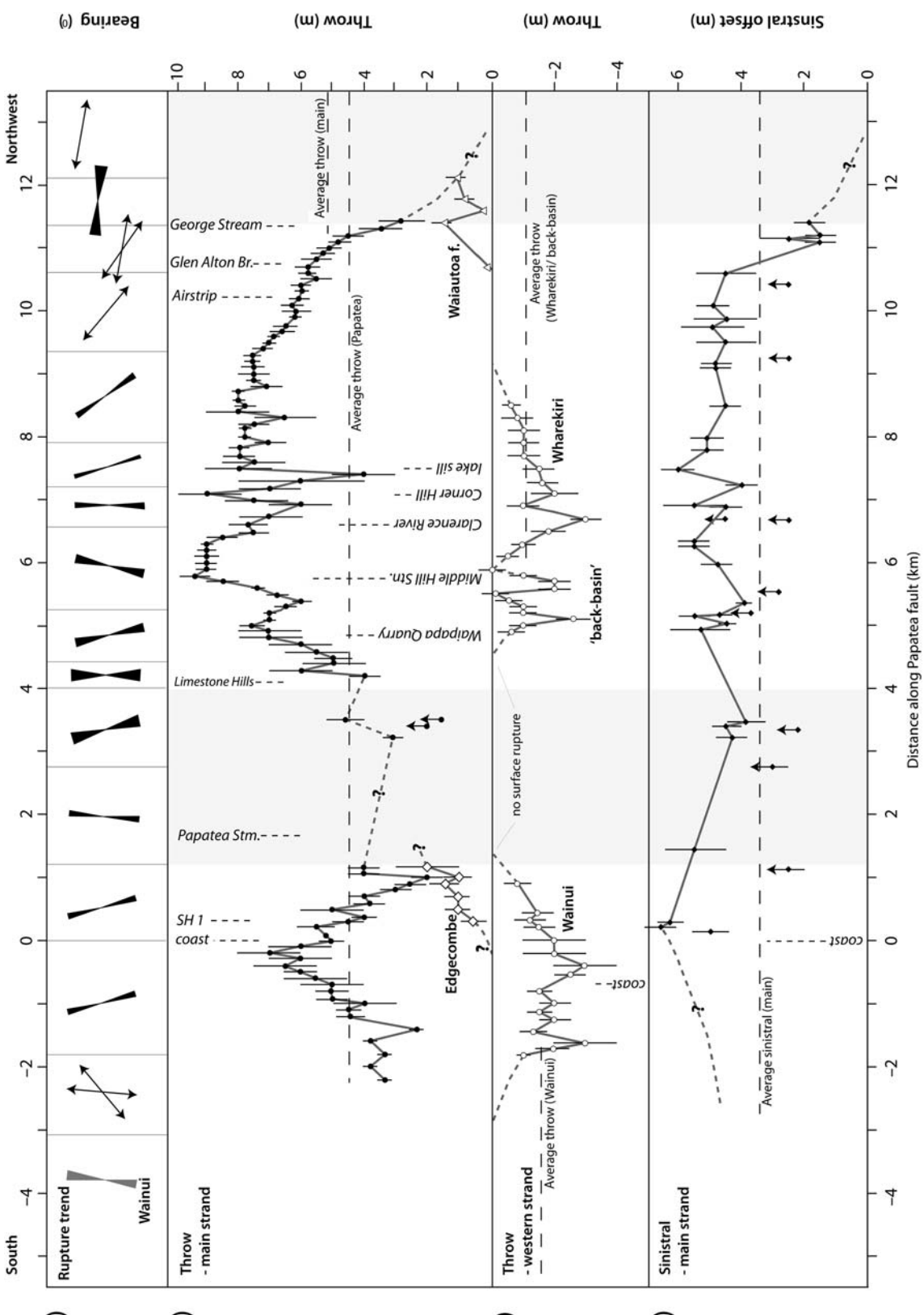

Figure 17. Rupture trend and offset data for the Papatea fault. Light gray vertical shading represents areas where there is no D-lidar data. The solid and dashed gray and dashed lines joining data are the interpreted slip distributions. *X* axis is in kilometers from the coast on the main strand, with local place names along-strike identified. Arrows on point data reflect minimum values. Average throws for each strand and an average throw for the Papatea fault are shown in (b) and (c). (a) Rupture trend along the main strand of the Papatea fault, with one offshore observation from the Wainui strand. Arrows define two distinct fault trend sets, and hourglasses define a range of rupture trend. (b) Up-to-the-west throw on the main strand and Edgecombe trace (diamonds). Waiautoa fault offsets (triangles) are projected into the plane of the Papatea fault strike. (c) Up-to-the-east throw on the western strand, shown as negative values because they are interpreted to have antithetic throw relative to the main strand. (d) Distribution of sinistral offset along the main strand of the fault. Data appears in Ⓔ Table S1.

Average and Net Slip Calculations for the Papatea Fault

The throw and strike-slip distributions can be used to estimate the average throw and average lateral offset. We used a method of integrating under the area of each offset distribution for each given strand presented in Figure 17. The average throw for the main strand is $\sim 5.1 \pm 0.3$ m. The average throws for the Wainui and Wharekiri traces are $\sim 1.9 \pm 0.1$ and $\sim 1.6 \pm 0.1$ m, respectively. We subtract the area of the western strand from the area of the main strand to determine the total throw area. This yields an average ground-surface throw of $\sim 4.5 \pm 0.3$ m for the Papatea fault. This is important because, as can readily be observed along the coast (Ⓔ Fig. S2; Clark *et al.*, 2017), the far-field throw across the Papatea fault is considerably less than observed across individual strands. The average sinistral slip is calculated in the same fashion and is $\sim 3.4 \pm 0.1$ m. The average slip calculations could represent minima, because our analysis included some minimum individual offset values from field data, for which we are lacking D-lidar coverage.

The net average slip, assessed in this case from the average throw and sinistral offset, combined with an average dip of 55° W is calculated as 6.4 ± 0.2 m, directed toward the south. These values do not consider the component of fault shortening (which would rotate the slip direction toward southeast) nor other uncertainties. The contributions from other faults discussed in this article, for example, from the Waiautoa fault (which is included in Fig. 17b), are ignored because they provide only a minor additional input to the maximum and average net slip related to the Papatea fault itself.

Discussion

Papatea Fault Slip and Papatea Block Motion

Coseismic rupture of the Papatea fault is consistent with motions of both the hanging-wall Papatea block and footwall block in the Kaikōura earthquake and with the longer-term kinematics of the area from geology (Rattenbury *et al.*, 2006). Our field-, multibeam-, and lidar-derived results indicate that coseismic multimeter, reverse, and sinistral displacements measured across the Papatea fault (Fig. 17) are matched by, and help reconcile, the motion of the hanging-wall Papatea block (Fig. 2). Vertical displacement on the footwall block of the Papatea fault is generally negligible, whereas the horizontal motion of the footwall block is almost purely westward directed and multimeter in size (Hamling *et al.*, 2017). This component of block motion, in part resolved as minor east-vergent shortening evidenced from surface ruptures across both the Papatea and Waiautoa faults, is also consistent with Interferometric Synthetic Aperture Radar (InSAR)/geodetic studies. Our estimates of the maximum and average displacements along the Papatea fault are consistent with, and provide higher resolution to, regional-to-local scale displacement models derived from InSAR/GPS, optical-image correlation, and aerial photo correlation techniques. Hamling *et al.* (2017) record ~8 m of relative uplift and 4–6 m of south- to southeast translation for the Papatea block, whereas Mackenzie *et al.* (2017) record ~6–10 m of relative uplift and 5–6 m of south- to south-southwest-directed translation of the Papatea block. These motions are largely resolved by motion on the Papatea fault. Kääb *et al.* (2017) and Klinger *et al.* (2017) present horizontal motions of ~6.5 m to the southeast and ~4–6 m to the south to southeast, respectively, for the Papatea block, consistent with sinistral motion measured across the Papatea fault.

The kinematics of the Papatea block is not the main topic of this article and will be explored in future research that exploits the full 3D deformation field enabled by pre- and postevent lidar (e.g., Nissen *et al.*, 2017). However, insights gained from wider-scale reconnaissance mapping (e.g., Langridge *et al.*, 2017; Kearse *et al.*, 2018; Litchfield *et al.*, 2018) and InSAR/GPS and optical correlations models (e.g., Hamling *et al.*, 2017; Mackenzie *et al.*, 2017) inform that motion of the Papatea block during the Kaikōura earthquake (1) must be resolved not only onto its eastern boundary fault (the Papatea fault but also onto the other block-bounding faults, including the Jordan thrust and Hope fault, and (2) must also reflect complex block motions and interactions including rotation, oblique block uplift and escape, response to space problems and internal deformation (e.g., the SCF), and neighboring block/microblock motions. The large uplift and southward translation of the Papatea block may be a consequence of space problems; it is a wedge-shaped block sandwiched between the Jordan thrust (that ruptured in 2016) and the Hope fault that resisted rupture in 2016. The large uplift of the Papatea block could also be explained by the changes in fault dip with depth or intersection with a dipping structure at shallow to moderate depth within the crust beneath it, as suggested by Cesca *et al.* (2017).

Similarly, an important lesson from the 2016 Kaikōura earthquake has been in understanding the upper crustal structure and the inheritance of structure within the largely homogenous Cretaceous Pahau graywacke basement across the northeastern South Island. Several faults involved in the Kaikōura earthquake including the Papatea, Leader, Stone Jug, and Whites faults are north- to north-northwest-striking reverse sinistral or sinistral reverse faults (Litchfield *et al.*, 2018; Nicol *et al.*, 2018; this study). Prior to 2016, none of these faults had been mapped as active, that is, with recognizable activity over the last 125,000 yrs according to the NZAFD (Langridge *et al.*, 2016). This is probably due to a lack of mapped active fault traces across latest Pleistocene and Holocene geomorphic surfaces, which points to the possibility that these faults individually have long recurrence intervals ($\geq$ 5000–10,000 yrs) or only rupture in complex multisegment ruptures (Litchfield *et al.*, 2018). Thus, the Papatea block is one of several fault-bounded upper crustal microblocks that was activated in the 2016 Kaikōura earthquake, being bounded by rhombic arrays of active northeast-

Table 1
Rupture Parameters of Some Very Large to Great Historical Reverse/Strike-Slip Earthquakes

Earthquake	M_w	Fault Length (km)	Maximum Throw (m)	Maximum Slip (m)	Mean Slip (m)	References
1855 Wairarapa	~8.2	about 140	6	18	—	Grapes and Downes (1997) and Rodgers and Little (2006)
1957 Gobi-Altay	7.9–8.1	260	4	7	3.5–4	Choi *et al.* (2012) and Rizza *et al.* (2011)
1999 Chi-Chi	7.6	100	7.5	16.4	—	Lin *et al.* (2001) and Wesnousky (2008)
2008 Wenchuan	7.9	>240	6.5	6.7	—	Xu *et al.* (2009) and Yu *et al.* (2010)
2016 Kaikōura	7.8	165–180	9.5 ± 0.5	12	3–5	Litchfield *et al.* (2018) and this study
	(~7.2)*		9.5 ± 0.5	11.5 ± 2.0	6.4 ± 0.2	
Papatea fault	6.7†	17–19	1	1.4	0.7	Stirling *et al.* (2012)

*Magnitude calculated for the Papatea fault as part of the Kaikōura earthquake.
†Magnitude calculated for the Papatea fault as a single seismic source fault using Stirling *et al.* (2012).

striking dextral to reverse dextral-slip faults (e.g., Hundalee, Jordan, and Kekerengu), linked together by north- to north-northwest-striking, reverse sinistral or sinistral reverse faults in a transpressional setting.

In light of the Kaikōura earthquake, the previously unknown Papatea fault (and Papatea block) clearly has an important role in the local plate-boundary kinematics in the complex transition from the Hope fault to the Kekerengu fault and ultimately to the HSM. The north-striking sinistral reverse Papatea fault is an important linking fault between these high slip-rate faults, prompting re-evaluations of the role of active faults in this region in terms of seismic hazard.

Seismic Hazard Implications of Large Coseismic Displacements

Field measurements complement models developed from seismologic and geodetic datasets discussed earlier. The maximum and average net slip calculations for the Papatea fault presented in this article are extraordinarily large, particularly for such a short fault, which has implications for seismic hazard. The maximum net oblique slip for the Papatea fault is ~11.5 ± 2 m, and the average net slip is ~6.4 ± 0.2 m. The former value is coequal to the largest slip recorded in the Kaikōura earthquake: ~12 m dextral slip on the Kekerengu fault (Kearse *et al.*, 2018). This highlights that the two largest fault slips occurred among the MFS faults (Kaiser *et al.*, 2017; Litchfield *et al.*, 2018) and are consistent with seismic moment release being larger in the second half of the earthquake process (Holden *et al.*, 2017; Zhang *et al.*, 2017).

The very large displacement values for the Papatea fault, as part of the Kaikōura earthquake rupture sequence, warrant a comparison to several other very large to great historical earthquakes. To consider length-versus-slip relationships, we compared the maximum throw and slip of the Papatea fault with several historical earthquake examples from long reverse/thrust fault or oblique transpressive earthquake ruptures (Table 1). Maximum and average Papatea fault displacements are as large as or larger than those observed in other historical examples. These examples include the 1999 M_w ~ 7.6 Chi-Chi, Taiwan, earthquake that ruptured the Chelungpu fault with maximum throws of ~7.5 m (Lin *et al.*, 2001; Wesnousky, 2008), the 2008 M_w ~ 7.9 Wenchuan, China, earthquake that involved vertical throw across the Beichuan fault of ~6.5 m (Xu *et al.*, 2009; Yu *et al.*, 2010), and the 1957 M_w 7.7–8.1 Gobi-Altay earthquake (Okal, 1977; Rizza *et al.*, 2011; Choi *et al.*, 2012). In the southern North Island, vertical throw on part of the Wairarapa fault system uplifted Cape Turakirae beach ridges by ~6 m during the 1855 M_w ~ 8.2 Wairarapa earthquake (Grapes and Downes, 1997; Little *et al.*, 2010; Schermer *et al.*, 2009). Our results suggest that the maximum throw on the Papatea fault (9.5 ± 0.5 m) is as large as any known on land historic fault rupture of this style. What is so outstanding about this observation is that the length of the Papatea fault (17–19 km) is short compared with the length of these surface ruptures, especially given the expectations of slip per fault length (e.g., Wells and Coppersmith, 1994). Because of its location between the Jordan-Kekerengu and Hope faults and its role as a linking fault between them, the Papatea fault is undoubtedly length limited in terms of generating seismic moment. Therefore, it seems likely that such large displacements must be generated as part of a larger multifault or multisegment earthquake in which magnitude and length scale to very large values (Litchfield *et al.*, 2018). These observations on prehistoric ruptures probably point to the presence of multifault ruptures and should be considered for fault source characterizations in seismic hazard studies.

Although the Papatea fault is short and has not been modeled as an elastic fault source in some published models (Clark *et al.*, 2017; Hamling *et al.*, 2017), geologic surface slip data indicate that it was indeed involved as part of a more complex multifault earthquake rupture (Litchfield *et al.*, 2018). In terms of seismic hazard, one of the questions we wish to answer is: Is involvement in a multifault Kaikōura-type earthquake rupture the norm for the Papatea fault, or can it rupture on its own? If we consider the Papatea fault as an ~18-km-long single-segment rupture and follow the method for single-fault source characterization used in the 2010 New Zealand Seismic Hazard Model (NSHM) based

on empirical fault scaling relationships (Stirling *et al.*, 2012), we obtain an earthquake of magnitude (M_w) 6.7 ± 0.1, yielding an average net slip of 1.3 ± 0.1 m. In contrast, the geologic moment derived for the Papatea fault in the Kaikōura earthquake from coseismic displacement measures is $M_w \sim 7.2$ (6.9–7.3) (Litchfield *et al.*, 2018).

The discrepancy between the calculated single-event displacement using the 2010 NSHM methodology (1.3 ± 0.1 m) and the average slip on the Papatea fault during the multifault Kaikōura earthquake (6.4 ± 0.2 m) raises another important question building upon the previous one: Is the slip observed on the Papatea fault during the Kaikōura earthquake characteristic of its behavior or can it also accrue minor (meter-scale) slip in single-segment events? If the former, the paleoslip record will be dominated by large throw/net-slip events. Conversely, if the latter, the slip history of the Papatea fault will include evidence for smaller events, arguably occurring more frequently. The implications for these inferences are discussed below in terms of the landscape legacy of the Papatea fault and the Kaikōura earthquake and are being addressed in ongoing paleoseismic studies.

Geomorphic Legacy of the Papatea Fault Rupture and Kaikōura Earthquake

The 2016 Kaikōura earthquake and Papatea fault ruptures have left a significant geomorphic legacy in the lower Clarence River valley. This legacy includes: regional uplift of the landscape, most notably at the coast forming an uplifted horst; uplifted alluvial terraces and a bedrock strath within a wider extruded tectonic sliver; diversion (avulsion) of a major river creating a lake; very large landslides and extensive shattering of surrounding hill country; and of course coseismic fault rupture that has created a pronounced step in elevation from the west to east side of the valley (Clark *et al.*, 2017; Massey *et al.*, 2018; this study). The signals of the pre-Kaikōura legacy of the Papatea fault include: (1) uplifted late Pleistocene marine terraces and raised Holocene beach deposits on the hanging-wall side of the Papatea fault at the coast (Ota *et al.*, 1996; Clark *et al.*, 2017; Litchfield *et al.*, 2017); (2) hummocky terrain adjacent to the Limestone Hills landslide and near the Waipapa Quarry, which is indicative of previous large landslides from the limestone-dominated hill country above the Clarence Valley (Massey *et al.*, 2018); and (3) a suite of preserved uplifted alluvial terraces in the MHS area and in the lower Wharekiri Stream that attest to late Pleistocene to Holocene deformation preserved between the main and western strands of the Papatea fault.

However, there is little evidence for a pre-existing Holocene fault trace along any part of the Papatea fault in the Clarence Valley (Barrell, 2015), presumably because either (1) the Clarence River has significant stream power, and prior scarps are either eroded or buried by younger sediment; and/or (2) there is a relatively long recurrence time between multisegment Kaikōura-type earthquakes that include rupture of the Papatea fault.

Since the Kaikōura earthquake, preliminary estimates of the long-term slip rate of the Papatea fault of ~1–2 mm/yr of vertical motion or ~1.7 ± 0.4 mm/yr dip slip were developed for seismic hazard model updates. These slip-rate estimates are based on the current height of the two elevated alluvial terraces on the hanging wall of the fault at MHS that before the earthquake were ~30 ± 2 and 18 ± 2 m above the current fill terrace on the footwall side (e.g., Figs. 10 and 11a). These terraces are inferred to be the Last Glaciation and early Holocene alluvial terraces, with approximate ages of ~15–18,000 and 10–12,000 yr B.P., respectively, that are correlated regionally throughout New Zealand (e.g., Litchfield and Berryman, 2005). Despite the uncertainty associated with these age assignments, they suggest a vertical slip rate (~1–2 mm/yr) that would allow development of a flight of terraces separated as they are, but not such a fast slip rate that Holocene-age scarps would be expected to be preserved. With respect to mountain range geomorphology, we note that ranges in the North Canterbury region occur in landscapes characterized by rolling hills cored by Tertiary rocks, typically in association with faults of lower uplift/slip rate (Pettinga *et al.*, 2001; Litchfield *et al.*, 2014). In contrast, high elevation ranges in higher uplift rate areas in the South Island, such as the Southern Alps (2–12 mm/yr) and Seaward Kaikōura range (> 4 mm/yr), are bedrock cored and are stripped clean of Tertiary cover rocks (Van Dissen and Yeats, 1991; Norris and Cooper, 2001). Therefore, we infer from the range geomorphology of the Papatea block, that includes the intensely folded Late Cretaceous to Miocene sequence in the Puhipuhi Syncline, an intermediate uplift rate on the order of ~1–2 mm/yr.

From these inferences, and based on maximum throws of ≥ 8 m per event, it is reasonable to suggest that there may have been 1–2 prehistoric multisegment events involving the Papatea fault in the last 10–12,000 yrs and 2–4 such events in the last 15–18,000 yrs, that is, allowing for the uplift and preservation of terraces T1 and T2 on the hanging wall (Figs. 10 and 11a). Therefore, we tentatively suggest that multisegment earthquakes invoking Papatea fault rupture recur on time scales of ≥ 5000–12,000 yrs. Such a recurrence time is also suggested by Litchfield *et al.* (2018) for a repeat of a multisegment Kaikōura-type earthquake, using the recurrence intervals from low slip-rate faults in the NCD that ruptured in 2016. Alternatively, whereas single-segment meter-scale Papatea ruptures would have to recur repeatedly at the submillennial scale (calculation from the 2010 NSHM methodology yields an average recurrence time of ~800 yrs), we cannot rule out a combination of multi- and single-segment events for past or future ruptures of the Papatea fault. For interim seismic hazard model updates, combinations of single- and multisegment ruptures have been suggested that include rupture of the Papatea fault. At present, our preferred interpretation of the behavior of the Papatea fault is that it is typically

involved in multisegment ruptures, either with the Hope (Conway/offshore) or Jordan-Kekerengu fault systems (Stirling *et al.*, 2012; Kearse *et al.*, 2018).

The multisegment recurrence interval mode for the Papatea fault ($\geq$ 5000–12,000 yrs) suggested here is at least 10 times longer than recurrence intervals derived for either the Hope fault (180–310 yrs) or the Kekerengu fault (376 ± 32 yrs) from paleoseismic trenching or from the consideration of slip-rate and single-event displacement (Langridge *et al.*, 2003; Litchfield *et al.*, 2018; Little *et al.*, 2018). Similarly, the uplift rate we infer here for the Papatea fault (1–2 mm/yr) is at least an order of magnitude less than slip rates published for the Hope and Kekerengu faults (Langridge *et al.*, 2003; Litchfield *et al.*, 2014). These results imply that complex multifault ruptures are not typically the norm ($<$ 1 in every 10 Hope or Kekerengu fault events; see Litchfield *et al.*, 2018) and that the majority of plate boundary deformation must still be channeled from the Alpine fault via the Hope, Jordan, and Kekerengu faults to the HSM.

Returning to the landscape legacy of the Papatea fault and the Kaikōura earthquake, it is clear that a large river such as the Clarence River has played a key role in re-shaping the landscape toward equilibrium conditions since the penultimate Papatea fault rupture. We find little evidence for Holocene fault scarps in the Clarence Valley, demonstrating the ability of the river to re-shape its valley; although considering the large displacements in 2016, it may take many years or decades to reach equilibrium conditions.

Conclusions

Surface rupture of the sinistral reverse Papatea fault has been documented and displacements measured using a variety of onshore and offshore mapping tools, including multibeam, on-land and offshore lidar, and D-lidar. These data indicate that rupture of the oblique-slip Papatea fault is associated with unusually large displacements (maximum net slip of 11.5 ± 2 m; average net slip of 6.4 ± 0.2 m) for such a short fault (18 km). These observations have important implications for considering paleoslip and rupture models for fault networks for the purposes of fault-source characterization in seismic hazard studies.

Coseismic fault slip magnitude and direction for the Papatea fault are very consistent with InSAR/GPS and optically derived models of local block motions. These models indicate $\geq$ 8 m of uplift of the Papatea block. Coseismic throw across the Papatea fault in the near-field measures similarly high values compared to the uplift modeled across much of the Papatea block. The throw distribution peaks along the central part of the Papatea fault and tails to the northwest and southern ends, where the Papatea fault has junctions with the Jordan thrust and offshore Hope fault, respectively.

Coseismic sinistral slip observed across the Papatea fault is equivalent in scale and slip direction to the magnitude of block movements associated with the Papatea block. Where it was possible to measure, coseismic sinistral slip is consistently high (4–6 m; average ~3.4 m) along the length of the Papatea fault, matching quite well with the pattern of south- to southeast-directed block-motion vectors indicated from InSAR/geodesy. Such models confirm that the Papatea block, which essentially acted as a large compressional jog in the Kaikōura earthquake, moved by many meters both vertically and to the south to southeast relative to the footwall block of the Papatea fault.

Preliminary inferences of the vertical and dip-slip rates for the Papatea fault, consideration of the fault slip per length observed for the fault in the Kaikōura earthquake, and an assessment of the Holocene geomorphic expression of the fault all point to the recurrence interval of large ($\geq$ 8 m) throw events on the Papatea fault as being quite long ($\geq$ 5000–12,000 yrs). These inferences are consistent with other estimates that imply that the multisegment Kaikōura-type earthquake that links together faults of different strike, style, rate, and recurrence interval is probably a relatively infrequent event in the geologic record of the Marlborough region.

Data and Resources

A 1:250,000 scale map of the surface ruptures can be downloaded from the New Zealand Active Faults Database (https://data.gns.cri.nz/af/, choose the Download Data – Kaikōura option, last accessed May 2018). The remainder of datasets used comes from published sources listed in the References.

Acknowledgments

The authors wish to firstly thank the landowners in the Clarence Valley who were very open and helpful with our earthquake reconnaissance and subsequent field work, despite having experienced one of the largest on-land earthquakes in our history. For help in the field, the authors wish to acknowledge Brendan Hall, Jesse Kearse, Adrian Benson, Rob Zinke, and Tim Little who also provided fault attitude measurements from the coast. The authors also thank the reconnaissance support given by many helicopter pilots. Russ Van Dissen provided many useful discussions, and David Rhoades provided help determining average net slip calculations. Funding was provided by GeoNet with the support of its sponsors, New Zealand Earthquake Commission (EQC), GNS Science, and Land Information New Zealand, and Ministry of Business, Innovation and Employment (MBIE) response funding, provided through the Natural Hazards Research Platform (Grant Number 2017-GNS-01-NHRP), and GNS Science MBIE strategic science investment funding (GNS-SSIF-TSZ), which funded the extensive postearthquake light detection and ranging (lidar) acquisitions. Funding for the offshore fault mapping work with RV Ikatere was provided by MBIE through the Natural Hazards Research Platform (Grant Number C05X0907). Reviews by Nicola Litchfield, Phaedra Upton, Robert Zinke, Yann Klinger, and Kelvin Berryman helped to significantly improve the article. The authors also wish to thank the editorial team for their support.

References

Bai, Y., T. Lay, K. F. Cheung, and L. Ye (2017). Two regions of seafloor deformation generated the tsunami for the 13 November 2016, Kaikōura, New Zealand, earthquake, *Geophys. Res. Lett.* **44,** 6598–6606.

Barka, A., H. S. Akyüz, G. Sunal, Z. Çakir, A. Dikbaş, B. Yerli, E. Altunel, R. Armijo, B. Meyer, J. B. Chebalier, *et al.* (2002). The surface rupture and slip distribution of the 17 August 1999 İzmit earthquake, (M 7.4), North Anatolian fault, *Bull. Seismol. Soc. Am.* **92,** 43–60.

Barrell, D. J. A. (2015). General distribution and characteristics of active faults and folds in the Kaikōura District, North Canterbury, *GNS Science Consultancy Report 2014/210*, available at https://www.ecan.govt.nz/data/document-library/?ids=1645906, 1811999, 2147181, 1811995, 1512242, 1242237, 1394179, 1337380, 1059852, 301544, 1081016, 2250897 (last accessed May 2018).

Barrell, D. J. A., and D. B. Townsend (2012). General distribution and characteristics of active faults and folds in the Hurunui District, North Canterbury, *GNS Science Consultancy Report 2012/113*, available at https://www.ecan.govt.nz/data/document-library/?ids=1645906, 1811999, 2147181, 1811995, 1512242, 1242237, 1394179, 1337380, 1059852, 301544, 1081016, 2250897 (last accessed May 2018).

Cesca, S., Y. Zhang, V. Mouslopoulou, R. Wang, J. Saul, M. Savage, S. Heimann, S.-K. Kufner, O. Oncken, and T. Dahm (2017). Complex rupture process of the M_w 7.8, 2016, Kaikōura earthquake, New Zealand, and its aftershock sequence, *Earth Planet. Sci. Lett.* **478,** 110–120.

Choi, J.-H., K. Jin, D. Enkhbayar, B. Davvasambuu, A. Bayasgalan, and Y.-S. Kim (2012). Rupture propagation inferred from damage patterns, slip distribution, and segmentation of the 1957 M_w 8.1 Gobi-Altay earthquake rupture along the Bogd fault, Mongolia, *J. Geophys. Res.* **117,** no. B12401, doi: 10.1029/2011JB008676.

Clark, K., E. Nissen, J. Howarth, I. Hamling, J. Mountjoy, W. Ries, K. Jones, S. Goldstein, U. Cochran, P. Villamor, *et al.* (2017). Highly variable coastal deformation in the 2016 M_w 7.8 Kaikōura earthquake reflects rupture complexity along a transpressional plate boundary, *Earth Planet. Sci. Lett.* **474,** 334–344.

Cunningham, W. D., and P. Mann (2007). Tectonics of strike-slip restraining and releasing bends, in *Tectonics of Strike-Slip Restraining and Releasing Bends*, W. D. Cunningham and P. Mann (Editors), Vol. 290, Geological Society, London, United Kingdom, Special Publications, 1–12.

Dellow, S., C. Massey, S. Cox, G. Archibald, J. Begg, Z. Bruce, J. Carey, J. Davidson, F. Della Pasqua, P. Glassey, *et al.* (2017). Landslides caused by the M_w 7.8 Kaikōura earthquake and the immediate response, *Bull. New Zeal. Soc. Earthq. Eng.* **50,** 106–116.

Duputel, Z., and L. Rivera (2017). Long-period analysis of the 2016 Kaikōura earthquake, *Phys. Earth Planet. In.* **265,** 62–66.

Furlong, K. P., and M. Herman (2017). Reconciling the deformational dichotomy of the 2016 M_w 7.8 Kaikōura New Zealand earthquake, *Geophys. Res. Lett.* **44,** 6788–6791.

Grapes, R., and G. Downes (1997). The 1855 Wairarapa, New Zealand, earthquake—Analysis of historical data, *Bull. New Zeal. Soc. Earthq. Eng.* **30,** 271–368.

Haeussler, P. J., D. P. Schwartz, T. E. Dawson, H. D. Stenner, J. J. Lienkaemper, B. Sherrod, F. R. Cinti, P. Montone, P. A. Craw, A. J. Crone, *et al.* (2004). Surface rupture and slip distribution of the Denali and Totschunda faults in the 3 November 2002 M 7.9 earthquake, Alaska, *Bull. Seismol. Soc. Am.* **94,** S23–S52.

Hamling, I. J., S. Hreinsdóttir, K. Clark, J. Elliott, C. Liang, E. Fielding, N. Litchfield, P. Villamor, L. Wallace, T. J. Wright, *et al.* (2017). Complex multi-fault rupture during the 2016 M_w 7.8 Kaikōura earthquake, New Zealand, *Science* doi: 10.1126/science.aam7194.

Holden, C., Y. Kaneko, E. D'Anastasio, R. Benites, B. Fry, and I. J. Hamling (2017). The 2016 Kaikōura earthquake revealed by kinematic source inversion and seismic wavefield simulations: Slow rupture propagation on a geometrically complex crustal fault network, *Geophys. Res. Lett.* **22,** 11,320–11,328, doi: 10.1002/2017GL075301.

Kääb, A., B. Altena1, and J. Mascaro (2017). Coseismic displacements of the 14 November 2016 M_w 7.8 Kaikōura, New Zealand, earthquake using the Planet optical cubesat constellation, *Nat. Hazards Earth Syst. Sci.* **17,** 627–639, doi: 10.5194/nhess-17-627-2017.

Kaiser, A., N. Balfour, B. Fry, C. Holden, N. Litchfield, M. Gerstenberger, E. D'Anastasio, N. Horspool, G. McVerry, J. Ristau, *et al.* (2017). The Kaikōura, New Zealand, earthquake: Preliminary seismological report, *Seismol. Res. Lett.* **88,** no. 3, doi: 10.1785/0220170018.

Kamb, B., L. T. Silver, M. J. Abrams, B. A. Carter, T. H. Jordan, and J. B. Minster (1971). Pattern of faulting and nature of fault movement in the San Fernando earthquake, *U.S. Geol. Surv. Profess. Pap. 733*, 41–54.

Kearse, J., T. A. Little, R. J. Van Dissen, P. Barnes, R. Langridge, J. Mountjoy, W. Ries, P. Villamor, K. Clark, A. Benson, *et al.* (2018). Onshore to offshore ground-surface and seabed rupture of the Jordan–Kekerengu–Needles fault network during the 2016 M_w 7.8 Kaikōura earthquake, New Zealand, *Bull. Seismol. Soc. Am.* doi: 10.1785/0120170304.

Klinger, Y., J. Champenois, A. Delorme, K. Okubo, A. Vallage, H. Bhat, and S. Baize (2017). High-resolution optical-image correlation for the Kaikōura earthquake, slip distribution and rupture processes, *Proc. of the 8th International INQUA Meeting on Paleoseismology, Active Tectonics and Archeoseismology: Handbook and Programme*, K. J. Clark, P. Upton, R. Langridge, K. Kelly, and K. Hammond (Editors), 13–16 November 2017, GNS Science, Lower Hutt, New Zealand, 441 pp., GNS Science miscellaneous series 110, 206–209, doi: 10.21420/G2H061.

Langridge, R., J. Campbell, N. Hill, V. Pere, J. Pope, J. Pettinga, E. Estrada, and K. Berryman (2003). Paleoseismology and slip rate of the Conway Segment of the Hope fault at Greenburn stream, South Island, New Zealand, *Ann. Geophys.* **46,** 119–1139.

Langridge, R. M., W. F. Ries, N. J. Litchfield, P. Villamor, R. J. Van Dissen, D. J. A. Barrell, M. S. Rattenbury, D. W. Heron, S. Haubrook, D. B. Townsend, *et al.* (2016). The New Zealand active faults database, *New Zeal. J. Geol. Geophys.* **59,** 86–96.

Langridge, R., W. Ries, J. Rowland, P. Villamor, J. Kearse, T. Little, E. Nissen, C. Madugo, N. Litchfield, C. Gasston, *et al.* (2017). The role of surface-rupturing faults in the Waiautoa microblock, Clarence valley, New Zealand, during the M_w 7.8 2016 Kaikōura earthquake, *Proc. of the 8th International INQUA Meeting on Paleoseismology, Active Tectonics and Archeoseismology: Handbook and Programme*, K. J. Clark, P. Upton, R. Langridge, K. Kelly, and K. Hammond (Editors), 13–16 November 2017, GNS Science Miscellaneous Series 110, GNS Science, Lower Hutt, New Zealand, 445 pp., 216–219, doi: 10.21420/G2H061.

Lensen, G. J. (1962). Sheet 16 Kaikōura. Geological Map of New Zealand, scale 1:250,000, Dept. of Scientific and Industrial Research, Wellington, New Zealand.

Lin, A., T. Ouchi, A. Chen, and T. Maruyama (2001). Co-seismic displacements, folding and shortening structures along the Chelungpu surface rupture zone occurred during the 1999 Chi-Chi (Taiwan) earthquake, *Tectonophysics* **330,** 225–244.

Litchfield, N. J., and K. J. Berryman (2005). Correlation of late Quaternary river (fill) terraces in the eastern North Island, New Zealand: Implications for the relative effects of climate and baselevel controls on terrace formation in an actively uplifting tectonic setting, *Geomorphology* **68,** 291–313.

Litchfield, N., K. Clark, T. Miyauchi, K. Berryman, D. Barrell, L. Brown, Y. Ota, and T. Fujimori (2017). Holocene marine terraces record long-term uplift along the Kaikōura coastline, *Proc. of the 8th International INQUA Meeting on Paleoseismology, Active Tectonics and Archeoseismology: Handbook and Programme*, K. J. Clark, P. Upton, R. Langridge, K. Kelly, and K. Hammond (Editors), 13–16 November 2017, GNS Science, Lower Hutt, New Zealand, 441 pp., GNS Science miscellaneous series 110, 245–247, doi: 10.21420/G2H061.

Litchfield, N. J., R. Van Dissen, R. Sutherland, P. M. Barnes, S. Cox, R. Norris, J. Beavan, R. Langridge, P. Villamor, K. Berryman, *et al.* (2014). A model of active faulting in New Zealand, *New Zeal. J. Geol. Geophys.* **57,** 32–56.

Litchfield, N. J., P. Villamor, R. J. Van Dissen, A. Nicol, P. M. Barnes, D. J. A. Barrell, J. R. Pettinga, R. M. Langridge, T. A. Little, J. J. Mountjoy, *et al.* (2018). Surface rupture of multiple crustal faults in the 2016 M_w 7.8 Kaikōura, New Zealand, earthquake, *Bull. Seismol. Soc. Am.* doi: 10.1785/0120170300.

Little, T. A., R. Van Dissen, J. Kearse, K. Norton, A. Benson, and N. Wang (2018). Kekerengu fault, New Zealand: Timing and size of Late Holocene surface ruptures, *Bull. Seismol. Soc. Am.* doi: 10.1785/0120170152.

Little, T. A., R. Van Dissen, U. Rieser, E. G. C. Smith, and R. M. Langridge (2010). Coseismic strike slip at a point during the last four earthquakes on the Wellington fault near Wellington, New Zealand, *J. Geophys. Res.* **115,** no. B05403, doi: 10.1029/2009JB006589.

Mackenzie, D., and A. Elliott (2017). Untangling tectonic slip from the potentially misleading effects of landform geometry, *Geosphere* **13,** doi: 10.1130/GES01386.1.

Mackenzie, D., J. Elliott, E. Rhodes, S. Lamb, and B. Parsons (2017). Surface displacements in the 2016 Kaikōura earthquake derived from multi-scale optical data, *Proc. of the 8th International INQUA Meeting on Paleoseismology, Active Tectonics and Archeoseismology: Handbook and Programme*, K. J. Clark, P. Upton, R. Langridge, K. Kelly, and K. Hammond (Editors), 13–16 November 2017, GNS Science, Lower Hutt, New Zealand, 441 pp., GNS Science miscellaneous series 110, 256–259, doi: 10.21420/G2H061.

Massey, C., D. Townsend, E. Rathje, K. Allstadt, Y. Kaneko, B. Lukovic, B. Bradley, J. Wartman, N. Horspool, I. Hamling, *et al.* (2018). Landslides triggered by the 14 November 2016 M_w 7.8 Kaikōura earthquake, New Zealand, *Bull. Seismol. Soc. Am.* doi: 10.1785/0120170305.

Nicol, A., N. Khajavi, J. R. Pettinga, C. Fenton, T. Stahl, S. Bannister, K. Pedley, N. Hyland-Brook, T. Bushell, I. Hamling, *et al.* (2018). Preliminary geometry, displacement, and kinematics of fault ruptures in the epicentral region of the 2016 M_w 7.8 Kaikōura, New Zealand, earthquake, *Bull. Seismol. Soc. Am.* doi: 10.1785/0120170329.

Nissen, E., A. K. Krishnan, J. R. Arrowsmith, and S. Saripalli (2012). Three-dimensional surface displacements and rotations from differencing pre- and post-earthquake LiDAR point clouds, *Geophys. Res. Lett.* **39,** L16301, doi: 10.1029/2012GL052460.

Nissen, E., S. R. Malireddi, K. Clark, I. Hamling, R. Langridge, W. Ries, and A. Tagliasacchi (2017). Three-dimesnional coastal deformation in the M_w 7.8 Kaikōura earthquake from differntial airborne lidar, *Proc. of the 8th International INQUA Meeting on Paleoseismology, Active Tectonics and Archeoseismology: Handbook and Programme*, K. J. Clark, P. Upton, R. Langridge, K. Kelly, and K. Hammond (Editors), 13–16 November 2017, GNS Science, Lower Hutt, New Zealand, 441 pp., GNS Science miscellaneous series 110, 288–291, doi: 10.21420/G2H061.

Norris, R. J., and A. F. Cooper (2001). Late Quaternary slip rates and slip partitioning on the Alpine fault, New Zealand, *J. Struct. Geol.* **23,** 507–520.

Okal, E. A. (1977). The July 9 and 23, 1905, Mongolian earthquakes: A surface wave investigation, *Earth Planet. Sci. Lett.* **34,** 326–331.

Ota, Y., B. Pillans, K. Berryman, A. Beu, T. Fujimori, T. Miyauchi, and G. Berger (1996). Pleistocene coastal terraces of Kaikōura Peninsula and the Marlborough coast, South Island, New Zealand, *New Zeal. J. Geol. Geophys.* **39,** 51–73.

Pettinga, J. R., M. D. Yetton, R. J. Van Dissen, and G. Downes (2001). Earthquake source identification and characterisation for the Canterbury region, South Island, New Zealand, *Bull. New Zeal. Soc. Earthq. Eng.* **34,** 282–317.

Power, W., K. Clark, D. King, J. Borrero, J. Howarth, E. Lane, D. Goring, J. Goff, C. Chague-Goff, J. Williams, *et al.* (2017). Tsunami runup and tide-gauge observations from the 14 November 2016 M 7.8 Kaikōura earthquake, New Zealand, *Pure Appl. Geophys.* **174,** 2457–2473.

Rattenbury, M. S., D. B. Townsend, and M. R. Johnston (2006). Geology of the Kaikōura area, Institute of Geological & Nuclear Sciences, 1:250,000 geological map 13, 1 sheet + 70 pp., GNS Science, Lower Hutt, New Zealand.

Rizza, M., J.-F. Ritz, R. Braucher, R. Vassallo, C. S. Prentice, S. Mahan, S. McGill, A. Chauvet, S. Marco, M. Todbileg, *et al.* (2011). Slip rate and slip magnitudes of past earthquakes on the Bogd left-lateral strike fault (Mongolia), *Geophys. J. Int.* **186,** 897–927.

Rockwell, T. K., S. Lindvall, T. Dawson, R. Langridge, W. Lettis, and Y. Klinger (2002). Lateral offsets on surveyed cultural features from the 1999 İzmit and Düzce earthquakes, Turkey, *Bull. Seismol. Soc. Am.* **92,** 79–94.

Rodgers, D. W., and T. A. Little (2006). World's largest coseismic strike-slip offset: The 1855 rupture of the Wairarapa fault, New Zealand, and implications for displacement/length scaling of continental earthquakes, *J. Geophys. Res.* **111,** no. B12408, doi: 10.1029/2005JB004065.

Schermer, E. R., T. A. Little, and U. Rieser (2009). Quaternary deformation along the Wharekauhau fault system, North Island, New Zealand: Implications for an unstable linkage between active strike-slip and thrust faults, *Tectonics* **28,** doi: 10.1029/2008TC002426.

Stirling, M. W., N. J. Litchfield, P. Villamor, R. J. Van Dissen, A. Nicol, J. Pettinga, P. Barnes, R. M. Langridge, T. Little, D. J. A. Barrell, *et al.* (2017). The M_w 7.8 Kaikōura earthquake: Surface rupture, and seismic hazard context, *Bull. New Zeal. Soc. Earthq. Eng.* **50,** 73–84.

Stirling, M. W., G. McVerry, M. Gerstenberger, N. Litchfield, R. Van Dissen, K. Berryman, P. Barnes, L. Wallace, B. Bradley, P. Villamor, *et al.* (2012). National seismic hazard model for New Zealand: 2010 update, *Bull. Seismol. Soc. Am.* **102,** 1514–1542.

Vallage, A., Y. Klinger, R. Grandin, H. S. Bhat, and M. Pierrot-Deseilligny (2015). Inelastic surface deformation during the 2013 M_w 7.7 Balochistan, Pakistan, earthquake, *Geology* **43,** 1079–1082, doi: 10.1130/G37290.1.

Van Dissen, R., and R. S. Yeats (1991). Hope fault, Jordan thrust and uplift of the Seaward Kaikōura range, New Zealand, *Geology* **9,** 393–396.

Van Dissen, R., T. Stahl, A. King, C. Fenton, M. Stirling, N. Litchfield, T. Little, J. Pettinga, R. Langridge, A. Nicol, *et al.* (2018). Impacts of surface rupture on residential structures and rural infrastructure during the 14 November 2016 M_w 7.8 Kaikōura earthquake, New Zealand, *Proc. of the New Zealand Society for Earthquake Engineering Annual Conf.* 46**,** 1–8.

Wallace, L. M., P. Barnes, J. Beavan, R. Van Dissen, N. Litchfield, J. Mountjoy, R. Langridge, G. Lamarche, and N. Pondard (2012). The kinematics of a transition from subduction to strike-slip: An example from the central New Zealand plate boundary, *J. Geophys. Res.* **117,** no. B02405, doi: 10.1029/2011JB008640.

Wallace, L. M., J. R. Beavan, R. McCaffrey, K. R. Berryman, and P. Denys (2007). Balancing the plate motion budget in the South Island, New Zealand using GPS, geological and seismological data, *Geophys. J. Int.* **168,** 332–352, doi: 10.1111/j.1365-246X.2006.03183.x.

Wang, T., S. Wei, X. Shi, Q. Qiu, L. Li, D. Peng, R. J. Weldon, and S. Barbot (2018). The Kaikōura earthquake: Simultaneous rupture of the subduction interface and overlying faults, *Earth Planet. Sci. Lett.* **482,** 44–51.

Wells, D. L., and K. J. Coppersmith (1994). New empirical relationships among magnitude, rupture length, rupture width, rupture area, and surface displacement, *Bull. Seismol. Soc. Am.* **84,** 974–1002.

Wesnousky, S. G. (2008). Displacement and geometrical characteristics of earthquake surface ruptures: Issues and implications for seismic-hazard analysis and the process of earthquake rupture, *Bull. Seismol. Soc. Am.* **98,** 1609–1632.

Williams, J. N., D. J. A. Barrell, M. W. Stirling, K. M. Sauer, G. C. Duke, and K. X. Hao (2018). Surface rupture of the Hundalee fault during the 2016 M_w 7.8 Kaikōura earthquake, *Bull. Seismol. Soc. Am.* doi: 10.1785/0120170291.

Xu, X., X. Wen, G. Yu, G. Chen, Y. Klinger, J. Hubbard, and J. Shaw (2009). Coseismic reverse- and oblique-slip surface faulting generated by the 2008 M_w 7.9 Wenchuan earthquake, China, *Geology* **37,** 515–518.

Yu, G., X. Xu, Y. Klinger, G. Diao, G. Chen, X. Feng, C. Li, A. Zhu, R. Yuan, T. Guo, *et al.* (2010). Fault-scarp features and cascading-rupture model for the Wenchuan earthquake (M_w 7.9), Eastern Tibetan Plateau, China, *Bull. Seismol. Soc. Am.* **100,** 2590–2614.

Zhang, H., K. D. Koper, K. Pankow, and Z. Ge (2017). Imaging the 2016 M_w 7.8 Kaikoura, New Zealand, earthquake with teleseismic *P* waves: A cascading rupture across multiple faults, *Geophys. Res. Lett.* **44,** 4790–4798, doi: 10.1002/2017GL073461.

GNS Science
P.O. Box 30-368
Lower Hutt 5040
New Zealand
R.Langridge@gns.cri.nz
(R.M.L., P.V., D.B.T., W.F.R., I.H.)

The University of Auckland
Private Bag 92019
Auckland 1142
New Zealand
(J.R., C.G., A.C.)

National Institute of Water and Atmospheric Research
301 Evans Bay Parade
Wellington 6021
New Zealand
(J.M.)

School of Earth and Ocean Sciences
Bob Wright Centre A405
University of Victoria
Victoria, British Colombia
Canada V8P 5C2
(E.N.)

Pacific Gas and Electric Company
P.O. Box 997300
Sacramento, California 95899-7300
(C.M.)

University of Southern California
3651 Trousdale Parkway
Los Angeles, California 90089
(A.E.H.)

Manuscript received 9 November 2017;
Published Online 12 June 2018